

1 (2)

2 **Solar wind interaction with the Martian upper**  
3 **atmosphere: Crustal field orientation, solar cycle and**  
4 **seasonal variations**

Chuanfei Dong,<sup>1</sup> Stephen W. Bougher,<sup>1</sup> Yingjuan Ma,<sup>2</sup> Gabor Toth,<sup>1</sup> Yuni  
Lee,<sup>1</sup> Andrew F. Nagy,<sup>1</sup> Valeriy Tenishev,<sup>1</sup> Dave J. Pawlowski,<sup>3</sup> Michael R.  
Combi,<sup>1</sup> and Dalal Najib<sup>4</sup>

---

Corresponding author: C. F. Dong, Department of Atmospheric, Oceanic and Space Sciences,  
University of Michigan, Ann Arbor, Michigan, USA. (dcfy@umich.edu)

<sup>1</sup>Department of Atmospheric, Oceanic  
and Space Sciences, University of Michigan,  
Ann Arbor, Michigan, USA.

<sup>2</sup>Department of Earth and Space Sciences,  
UCLA, Los Angeles, California, USA.

<sup>3</sup>Department of Physics and Astronomy,  
Eastern Michigan University, Ypsilanti,  
Michigan, USA.

<sup>4</sup>National Academy of Sciences,  
Washington, D.C., USA.

**This is the author manuscript accepted for publication and has undergone full peer review but has not been through the copyediting, typesetting, pagination and proofreading process, which may lead to differences between this version and the Version of Record. Please cite this article as doi:**

D 10.1029/JGRA.52040

August 12, 2015, 6:02pm

D R A F T

5 **Abstract.** A comprehensive study of the solar wind interaction with the  
6 Martian upper atmosphere is presented. Three global models: the 3-D Mars  
7 multi-fluid Block Adaptive Tree Solar-wind Roe Upwind Scheme (BATS-R-  
8 US) MHD code (MF-MHD), the 3-D Mars Global Ionosphere Thermosphere  
9 Model (M-GITM) and the Mars exosphere Monte Carlo model Adaptive Mesh  
10 Particle Simulator (M-AMPS) were used in this study. These models are one-  
11 way coupled, i.e., the MF-MHD model uses the 3-D neutral inputs from M-  
12 GITM and the 3-D hot oxygen corona distribution from M-AMPS. By adopt-  
13 ing this one-way coupling approach, the Martian upper atmosphere ion es-  
14 cape rates are investigated in detail with the combined variations of crustal  
15 field orientation, solar cycle and Martian seasonal conditions.

16 The calculated ion escape rates are compared with Mars Express (MEX)  
17 observational data and show reasonable agreement. The variations in solar  
18 cycles and seasons can affect the ion loss by a factor of  $\sim 3.3$  and  $\sim 1.3$ , re-  
19 spectively. The crustal magnetic field has a shielding effect to protect Mars  
20 from solar wind interaction, and this effect is the strongest for perihelion con-  
21 ditions, with the crustal field facing the Sun. Furthermore, the fraction of  
22 cold escaping heavy ionospheric molecular ions  $[(\text{O}_2^+$  and/or  $\text{CO}_2^+)/\text{Total}]$  are  
23 inversely proportional to the fraction of the escaping (ionospheric and corona)  
24 atomic ion  $[\text{O}^+/\text{Total}]$ , whereas  $\text{O}_2^+$  and  $\text{CO}_2^+$  ion escape fractions show a pos-  
25 itive linear correlation since both ion species are ionospheric ions that fol-  
26 low the same escaping path.

## 1. Introduction

27 The Sun has a powerful influence on planetary atmospheres. Annual changes in tem-  
28 perature on a planet are caused by a combination of two factors: axial tilt and variations  
29 in the distance from the Sun. On Earth, the axial tilt determines nearly all of the an-  
30 nual variations, because Earth's orbit is nearly circular. Mars, however, has the highest  
31 orbital eccentricity of any planet except Mercury; the distance from the Sun to Mars  
32 varies approximately from 1.38 AU to 1.66 AU over a Martian year. This large variation,  
33 combined with an axial tilt ( $25.19^\circ$ ) slightly greater than Earth's ( $23.4^\circ$ ), gives rise to sea-  
34 sonal variations far greater than those we experience even in the coldest areas on our own  
35 planet [*de Pater and Lissauer, 2010*]. Furthermore, Mars has no global intrinsic dipole  
36 magnetic field; instead, it has a crustal magnetic field, which was first discovered by the  
37 Mars Global Surveyor spacecraft (MGS) [*Acuña et al., 1999*]. The crustal fields,  $B_c$ , are  
38 distributed about the surface of the planet in a very inhomogeneous manner, which plays  
39 an important role in the process of solar wind planet interaction. The strongest crustal  
40 sources are located at latitudes poleward of  $30^\circ$  S and at longitudes between  $120^\circ$ – $240^\circ$   
41 E [*Acuña et al., 1999*].

42 Atmospheric dynamics and chemistry are greatly affected by temperature, suggesting  
43 that the entire Mars atmosphere is an integrated system that must be treated as a whole  
44 from the ground to the exobase ( $\sim 0$  to 250 km) [*Bougher et al., 2015*]. In fact, strong  
45 coupling processes are known to link the Mars lower to upper atmospheres [e.g., *Bougher*  
46 *et al., 2014*]. These processes are crucial to be quantified in order to reliably predict  
47 upper atmosphere densities, temperatures, winds, planetary waves (e.g., tides and gravity

48 waves) over various timescales (e.g. solar cycle, seasonal, and diurnal). Three-dimensional  
49 “whole atmosphere” models are ultimately required to capture these coupling processes  
50 (e.g., thermal, chemical, dynamical) throughout the entire Mars atmosphere. The 3-D  
51 Mars Global Ionosphere Thermosphere Model (M-GITM) [Bougher *et al.*, 2015] is such a  
52 model that can generate a relatively realistic Martian atmosphere with detailed structures  
53 that incorporates the effects of solar cycle and seasonal variations. Cold neutral atoms and  
54 molecules in this paper refer to the thermal particles, and hot oxygen refers to those from  
55 dissociative recombination of  $O_2^+$ . Basically, the hot oxygen has a thermal speed larger  
56 than the local background thermal speed (calculated based on M-GITM thermospheric  
57 profile [Bougher *et al.*, 2015]), indicating the scale height of hot oxygen is larger than that  
58 of the cold oxygen (e.g., Figures 1 and 2 in Ma *et al.* [2004]). However, the hot oxygen  
59 can be converted to the thermal oxygen via collisions with other background cold neutral  
60 species before it escapes to interplanetary space [Lee *et al.*, 2013]. It is noteworthy that  
61 when we mention the cold heavy ionospheric molecular/atomic ions, it refers to those  
62 ionized from the cold molecular/atomic neutrals. However, these ions can be accelerated  
63 to relatively high energy during their escape.

64 The weak gravity of Mars allows an extended corona of hot species to be present [Valeille  
65 *et al.*, 2009]. Among all the chemical reactions, dissociative recombination of  $O_2^+$  ( $O_2^+ +$   
66  $e \rightarrow O + O + \text{energy}$ ) is the most important one, which is responsible for most of  
67 the production of dayside exospheric hot atomic oxygen. Besides, the sputtering caused  
68 by pickup ion (e.g.,  $O^+$ ) collisions with the Martian atmospheric neutral species is also  
69 an important source for the hot corona [Johnson and Luhmann, 1998]. There are hot  
70 hydrogen and carbon coronae as well [Lee *et al.*, 2014a].

71 The cold exospheric component (e.g., see *Ma et al.* [2004] Figures 1 and 2) also plays  
72 an important role in the solar wind interaction with the Martian upper atmosphere, espe-  
73 cially below 600 km [*Feldman et al.*, 2011]. In order to reproduce a realistic asymmetric  
74 corona of hot species from observations, a 3-D global kinetic exosphere model is required,  
75 especially above the exobase (Knudsen number,  $K_n \approx 1$ ) where the fluid assumption usu-  
76 ally fails [*Lee et al.*, 2013]. One such model is the Mars exosphere Monte Carlo model  
77 Adaptive Mesh Particle Simulator (M-AMPS) [*Tenishev and Combi*, 2008; *Lee et al.*,  
78 2013, 2014a, b], which can generate a 3-D hot (e.g., oxygen and carbon) corona with  
79 detailed asymmetric structure. In order to capture these 3-D asymmetries, 3-D thermo-  
80 sphere/ionosphere inputs from a validated ground-to-exobase atmospheric model (e.g.,  
81 M-GITM) are essential (see Figure 1 for more details).

82 Over the last thirty years, a series of spacecrafts with plasma instrumentation have been  
83 sent to Mars, (e.g., Phobos 2, Mars Global Surveyor (MGS), and Mars Express (MEX)  
84 missions). The recent NASA Mars Atmosphere and Volatile EvolutioN (MAVEN) mission  
85 was launched on November 18, 2013, and successfully entered an orbit around Mars on  
86 September 21, 2014. MAVEN will explore the Mars upper atmosphere, ionosphere and  
87 interactions with the solar EUV radiation and solar wind environment, and determine the  
88 role that loss of volatiles to space has played through time. Recently, the study of the  
89 solar wind interaction with Mars upper atmosphere/ionosphere has received a great deal  
90 of attention, especially the investigation of ion escape rates due to its potential impact  
91 on the long-term evolution of Mars atmosphere (e.g., loss of water) over its history. A  
92 number of papers reporting on the measurement of ion escape rates by the ASPERA-3  
93 instrument on the Mars Express spacecraft have also been published [e.g., *Barabash et al.*,

94 2007; *Lundin et al.*, 2008, 2009, 2013; *Nilsson et al.*, 2011]. In *Lundin et al.* [2013], they  
95 reported that the average heavy ion escape rate is increased by a factor of  $\sim 10$ , from  $\sim$   
96  $1 \times 10^{24} \text{ s}^{-1}$  (solar minimum) to  $\sim 1 \times 10^{25} \text{ s}^{-1}$  (solar maximum). On the other hand, both  
97 *Verigin et al.* [1991] and *Nilsson et al.* [2011] suggested that high solar activity leads to  
98  $\sim 2.5$  times higher ion escape rate than the low solar activity result.

99 It is difficult to accurately estimate ion escape rates from spacecraft data due to the  
100 complex geometry of loss regions around Mars. Thus the use of global simulations is  
101 necessary. Various plasma models based on different assumptions, i.e., test particle model  
102 [*Fang et al.*, 2010; *Curry et al.*, 2013, 2014, 2015], multi-species MHD model [*Ma et al.*,  
103 2004; *Ma and Nagy*, 2007; *Ma et al.*, 2014], multi-fluid MHD model [*Harnett and Winglee*,  
104 2006; *Najib et al.*, 2011; *Riouisset et al.*, 2013, 2014; *Dong et al.*, 2014] and kinetic hybrid  
105 model [*Modolo et al.*, 2012; *Brecht and Ledvina*, 2014a] have been used to simulate the  
106 solar wind interaction with the Martian upper atmosphere and calculate the associated  
107 ion escape rates. An ongoing International Space Studies Institute effort focused upon the  
108 global models and measurements of the Martian plasma environment being led by Prof.  
109 David Brain at the University of Colorado, Boulder, CO [*Brain et al.*, 2010, 2012] allows  
110 intercomparison of these multidimensional plasma codes, which will benefit the entire  
111 community. However, there have been no systematic studies on the effects of crustal field  
112 orientation, solar cycle, and season on the Martian upper atmosphere ion escape by using  
113 the variable 3-D cold neutral thermosphere and hot oxygen corona as inputs in a plasma  
114 code.

115 In the present work, we study the solar wind interaction with the Martian upper atmo-  
116 sphere by using a one-way coupling of three comprehensive 3-D models, i.e., the M-GITM

117 thermosphere-ionosphere model outputs (i.e., neutral atmosphere temperatures  $T_n$ , neu-  
118 tral densities  $n_O$ ,  $n_{CO_2}$ , and photoionization frequencies  $I_O$ ,  $I_{CO_2}$ ) and the M-AMPS hot  
119 atomic oxygen corona densities ( $n_{O_{hot}}$ ) are used as inputs for the BATS-R-US Mars multi-  
120 fluid MHD (MF-MHD) model (see Figure 1 for the one-way coupling framework). The  
121 MF-MHD code solves separate continuity, momentum and energy equations for each ion  
122 species [Powell *et al.*, 1999; Glozer *et al.*, 2009; Najib *et al.*, 2011; Tóth *et al.*, 2012; Dong  
123 *et al.*, 2014]. Please refer to Lee *et al.* [2013, 2014a, b] for the detailed study of one-way  
124 coupling between M-GITM and M-AMPS (as indicated by the grey arrow in Figure 1),  
125 i.e., M-GITM provides neutral atmosphere background as an input into the M-AMPS  
126 exosphere model. These calculations are carried out for twenty-two cases with combina-  
127 tions of different crustal field orientations (four cases without crustal field), solar cycle  
128 and Martian seasonal conditions.

129 The rest of this paper is organized as follows. In Section 2, three models are briefly  
130 introduced together with the one-way coupling approach depicted in more detail. In  
131 Section 3, simulation results are presented and discussed based on the comparisons of 22  
132 selected cases. In the last section, conclusions are summarized.

## 2. Model Descriptions

133 In this section, we will briefly introduce the Mars Global Ionosphere Thermosphere  
134 Model (M-GITM) [Bougher *et al.*, 2015], the Mars exosphere Monte Carlo model Adaptive  
135 Mesh Particle Simulator (M-AMPS) [Lee *et al.*, 2013, 2014a, b], and the 3-D BATS-R-US  
136 Mars multi-fluid MHD (MF-MHD) model [Najib *et al.*, 2011; Dong *et al.*, 2014]. All these  
137 models are being used to generate a model library of simulated outputs for the MAVEN  
138 mission (2014-2016).

## 2.1. Mars Global Ionosphere Thermosphere Model (M-GITM)

Mars Global Ionosphere Thermosphere Model (M-GITM) [Bougher *et al.*, 2015] is a 3-D whole atmosphere code that captures both the Mars lower atmosphere and its thermosphere-ionosphere. The applied domain of this model is 0–250 km (ground-to-exobase). Lower, middle, and upper atmosphere processes are included, based in part upon formulations used in previous lower atmosphere (NASA AMES Mars General Circulation Model [e.g., Haberle *et al.*, 1999]) and upper atmosphere (NCAR Mars Thermospheric General Circulation Model [e.g., Bougher *et al.*, 2000]) models. The typical horizontal grid resolution of M-GITM is  $5^\circ \times 5^\circ$  (latitude-longitude) and the vertical coordinate is  $\Delta z=2.5$  km ( $\sim 0.25$  scale height). This model can calculate the neutral global fields including the temperatures ( $T_n$ ), and the neutral wind velocities ( $U_n$ ,  $V_n$ ,  $W_n$ ), where the vertical velocity is calculated explicitly for each species. The major neutral species are O, O<sub>2</sub>, CO<sub>2</sub>, CO, N<sub>2</sub>, Ar, and the minor neutral species, N(<sup>4</sup>S), N(<sup>2</sup>D), NO, He and H<sub>2</sub>, will be included soon. The major ions are CO<sub>2</sub><sup>+</sup>, O<sup>+</sup>, O<sub>2</sub><sup>+</sup>, N<sub>2</sub><sup>+</sup>, NO<sup>+</sup>, which are calculated assuming photochemical equilibrium. Sub-cycling is used for ion-neutral chemistry. Due to the relatively large scale height, hydrogen can only be calculated self-consistently by implementing the two-way coupling between the M-GITM and the M-AMPS models. Therefore, currently M-GITM does not include the calculation of hydrogen. There is no hydrostatic assumption in this model, thus it can deal with large vertical velocities [Ridley *et al.*, 2006; Deng *et al.*, 2008]. It is noteworthy that the previous Mars Thermospheric General Circulation Model (M-TGCM) is based on the hydrostatic assumption [Bougher *et al.*, 2000, 2006], and thus cannot deal with large vertical winds appropriately,



160 especially when experiencing extreme events, such as coronal mass ejections (CMEs) and  
161 solar energetic particles (SEPs) heating.

162 Detailed M-GITM simulations have been conducted over the past few years, spanning  
163 various seasonal, solar cycle, and dust conditions [*Bougher et al.*, 2015]. Model validation  
164 thus far has focused upon simulations for solar longitude  $L_s = 90, 180,$  and  $270$  for both  
165 solar minimum ( $F_{10.7} = 70$ ) and solar maximum ( $F_{10.7} = 200$ ) conditions. The solar  
166 longitude,  $L_s$ , is the Mars-Sun angle, measured from the northern hemisphere spring  
167 equinox, where  $L_s=0$ . Specific studies compare M-GITM simulated temperatures and  
168 neutral/ion densities against: (a) in-situ Viking 1 descent measurements for aphelion solar  
169 minimum conditions, and (b) very limited Mariner 6-7 flyby measurements for perihelion  
170 solar maximum conditions (see *Bougher et al.* [2015] for more details).

171 Figure 2 illustrates the  $\text{CO}_2$  and O densities on a sphere of altitude 220 km for these  
172 two extreme conditions. Interestingly, great day-night side asymmetry and detailed local  
173 structure are clearly shown in these four density contour plots, demonstrating the im-  
174 portance of adopting 3-D M-GITM neutral outputs. Besides, two coordinate systems are  
175 shown in Figure 2: the Geographic (GEO) and the Mars-centered Solar Orbital (MSO)  
176 coordinate systems. These plots are shown on a 2-D spherical surface with the rotation  
177 axis parallel to both  $x - z$  plane (in MSO coordinates) and the plane of the paper, where  
178 the subsolar point is highlighted in each plot. Clearly, there is an angle of 25.19 degrees  
179 between two  $z$  axes due to the axial tilt.

## 2.2. Mars Adaptive Mesh Particle Simulator (M-AMPS) model

180 The University of Michigan Adaptive Mesh Particle Simulator (AMPS) code was first  
181 developed to solve the Boltzmann equation of the gas flow in the coma of a comet [*Tenishev*

182 *and Combi*, 2008]. The AMPS code is developed within the framework of the Direct  
183 Simulation Monte Carlo (DSMC) method [*Bird*, 1994], which employs a stochastic solver  
184 for both the linear and nonlinear Boltzmann equations. As a standard numerical method  
185 today, the DSMC method can represent the collisional dynamics of a finite number of  
186 model particles in a rarefied gas flow regime, such as Mars upper atmosphere. Instead  
187 of solving the intractable Boltzmann equation, AMPS simulates the ensemble of model  
188 particles and captures the physics of the distribution of gas species in tenuous upper  
189 atmospheres, where the transitions from a local thermodynamic equilibrium (LTE) region  
190 to a non-LTE region occur. To model the Martian hot atomic coroneae, M-AMPS was run  
191 as a test-particle Monte Carlo model with a stationary background atmosphere supplied by  
192 M-GITM (as indicated by the dashed line in Figure 1), completing the one-way coupling  
193 framework [*Lee et al.*, 2013, 2014a, b]. Each hot particle in this coupling framework travels  
194 within the influence of the planet's gravitational field and collides with background species  
195 from M-GITM before escaping to space or being thermalized in the thermosphere. The  
196 nominal cell size is about 60 km at the lower boundary of the computational domain, and  
197 the maximum cell size is determined by the designated upper boundary of the domain.  
198 M-AMPS includes a data table, which keeps all the information from M-GITM. All the  
199 macro-particles in M-AMPS are initialized based on the thermospheric profile in the data  
200 table [*Lee et al.*, 2014a, b]. The collision frequencies between different particle species are  
201 also evaluated based upon the thermospheric information stored in the data table. The  
202 computational domain extends from 100 km above the Martian surface to  $5 R_M$ , where  
203  $R_M$  is the radius of Mars ( $\sim 3396$  km).

204 Recently, *Lee et al.* [2013, 2014a, b] have successfully finished the one-way coupling  
205 between M-AMPS and M-GITM (see Figure 1). This coupling approach has been used to  
206 calculate both the Martian exosphere hot atomic carbon and oxygen coronae [*Lee et al.*,  
207 2013, 2014a, b]. Figure 3 shows the hot atomic oxygen number density distribution in  
208 a logarithmic scale from the 3-D M-AMPS code. The upper panel shows the autumnal  
209 equinox solar minimum (AEQUMIN, left) and maximum (AEQUMAX, right) conditions  
210 and the bottom illustrates aphelion solar minimum (APHMIN, left) and perihelion solar  
211 maximum (PERMAX, right) conditions.

212 By comparing these four cases, the hot atomic oxygen corona is the most extensive  
213 and has the highest  $O_{hot}$  abundance for the PERMAX conditions, followed by the AE-  
214 QUMAX case; the hot atomic oxygen corona for the APHMIN conditions is the weakest.  
215 Furthermore, all these plots clearly show the asymmetric features of the hot atomic oxy-  
216 gen distribution, indicating that in order to accurately calculate the ion escape rate, it is  
217 essential to adopt the 3-D hot oxygen corona in a plasma code.

### 2.3. BATS-R-US Mars multi-fluid MHD (MF-MHD) model

218 The University of Michigan 3-D BATS-R-US multi-fluid MHD (MF-MHD) model was  
219 initially developed for Earth [*Powell et al.*, 1999; *Glocer et al.*, 2009; *Tóth et al.*, 2012] and  
220 later it was developed for studies of Mars [*Najib et al.*, 2011; *Dong et al.*, 2014]. The Mars  
221 MF-MHD model solves separate continuity, momentum and energy equations for the four  
222 ion fluids  $H^+$ ,  $O^+$ ,  $O_2^+$ ,  $CO_2^+$ . Although the multi-species MHD (MS-MHD) model solves  
223 separate ion continuity equations, it only solves one momentum and one energy equations  
224 for different ion species [*Ma et al.*, 2004]. Technically speaking, the MF-MHD model is  
225 more complete than the MS-MHD code [*Ma et al.*, 2004; *Ma and Nagy*, 2007] because

226 it can better simulate the solar wind planet interaction by considering the dynamics of  
227 individual ion species. The MS-MHD model, however, is computationally much cheaper  
228 than the MF-MHD model. In order to capture the dynamics of individual ion species, we  
229 adopt the MF-MHD model.

230 Different from the Earth version, the Mars MF-MHD model contains an ionosphere  
231 and thus the lower boundary (i.e., the spherical surface with the lowest altitude in the  
232 simulation domain) was extended down to 100 km above the Martian surface. Detailed  
233 ionospheric chemistry is included, i.e., charge exchange, photoionization and electron im-  
234 pact ionization. In order to calculate the latter, the model assumes that the electron  
235 temperature is half of the calculated plasma temperature and uses the ionization rates  
236 given by *Cravens et al.* [1987]. The same chemical reaction schemes in *Ma et al.* [2004] and  
237 *Najib et al.* [2011] are used, but with more realistic collision frequencies between species  
238 [*Schunk and Nagy*, 2009]. At the model lower boundary, the densities of  $O^+$ ,  $O_2^+$ ,  $CO_2^+$   
239 satisfy the photochemical equilibrium condition (refer to Chapters 8 and 13 (e.g., Figure  
240 13.1) of *Schunk and Nagy* [2009] for detailed ionospheric chemistry), and the velocity  $\mathbf{u}$  is  
241 set to satisfy a reflective boundary condition, which leads to approximately zero velocity  
242 at the inner boundary, as expected. At the inner boundary, both ions and electrons have  
243 roughly the same temperature as the neutrals due to collisions. Therefore, it is a reason-  
244 able assumption to set the plasma temperature to be twice the neutral temperature (i.e.,  
245  $T_{plasma} = T_i + T_e = 2T_n$ ). The crustal fields are implemented by the 60 degree harmonic  
246 expansion developed by *Arkani-Hamed* [2001], which can well describe the observed fields  
247 at Mars [*Acuña et al.*, 1999] and is particularly good at the MGS altitude ( $\sim 400$  km).  
248 A nonuniform, spherical grid structure is used in the model, where the radial resolution

249 varies from 5 km ( $\sim 0.5$  scale height, i.e., the vertical distance over which the density and  
250 pressure fall by a factor of  $1/e$ ) at the lower boundary ( $\sim 100$  km) to 1000 km at the outer  
251 boundary ( $\sim 20 R_M$ ). The angular resolution varies from  $1.5^\circ$  to  $3.0^\circ$ . The simulation  
252 domain is defined by  $-24 R_M \leq X \leq 8 R_M$ ;  $-16 R_M \leq Y, Z \leq 16 R_M$ .

253 Recently, *Dong et al.* [2014] successfully employed a one-way coupling between the  
254 MF-MHD model and the 3-D M-TGCM model [*Bougher et al.*, 2000, 2006] along with  
255 a 1-D spherically symmetric hot corona model [*Kim et al.*, 1998] to study the effects  
256 of the 3-D cold neutral atmosphere on ion escape rates. However, *Dong et al.* [2014]  
257 did not investigate the effects of varying inhomogeneous crustal field orientations and  
258 seasons on the Martian upper atmosphere ion loss. Moreover, as we described above, the  
259 M-TGCM model may not be able to handle the extreme cases (i.e., resulting in large  
260 vertical velocities) due to the hydrostatic assumption. M-TGCM is an upper atmosphere  
261 model which takes the NASA Ames Mars General Circulation Model outputs as its lower  
262 boundary conditions [see *Bougher et al.*, 2008].

263 The MF-MHD model uses a nonuniform spherical grid in MSO coordinate system, M-  
264 GITM uses a uniform spherical grid in GEO coordinate system, and M-AMPS adopts  
265 a nonuniform Cartesian grid in GEO coordinate system. In order to one-way couple  
266 the MF-MHD model with M-GITM and AMPS, we first need to carry out a coordinate  
267 transformation and linear interpolation between different grids. For the hot atomic oxy-  
268 gen, the AMPS output is able to cover the MF-MHD simulation domain from 100 km  
269 to  $5 R_M$ . For the M-GITM cold neutral profiles, we use the linear interpolation to cover  
270 the MF-MHD domain from 100 km to 220 km. From 220 km to  $5 R_M$ , we assume con-  
271 stant neutral temperatures and photoionization frequencies, based on the M-GITM values

272 since these values are almost constant when approaching 220 km. For the neutral atmo-  
273 sphere densities, however, we use an extrapolation based upon the hydrostatic assumption  
274 which assumes the neutral atmosphere densities decrease exponentially with altitude, i.e.,  
275  $n=n_0 \exp(-dz/H)$ , where  $dz$  is the altitude change and  $H$  is the scale height (which depends  
276 on the gravity, neutral temperature and neutral species mass). Technically speaking, the  
277 hydrostatic assumption may not be accurate enough to describe the cold oxygen compo-  
278 nent in the Martian exosphere, which should dominate the hot component up to 600 km  
279 in altitude [*Feldman et al.*, 2011]. However, the comparison of model results (from the  
280 one-way coupling between M-GITM and M-AMPS, Lee et al., 2015, submitted to JGR)  
281 and ALICE/Rosetta observations of the OI 1304 Å brightness [*Feldman et al.*, 2011] shows  
282 good agreement with each other on the transition altitude from cold to hot oxygen (~  
283 600 km), indicating that our extrapolation approach is reasonable. It is noteworthy that  
284 the cold oxygen component also plays an important role in the solar wind Mars interac-  
285 tion, especially below 600 km. The cold and hot corona components should be able to  
286 be calculated self-consistently in the future by adopting the two-way coupling approach  
287 (Figure 1).

### 3. Simulation Results and Discussion

288 In this section, we discuss the simulation results by implementing the one-way coupling  
289 approach mentioned in Section 2, i.e., both the M-GITM and AMPS 3-D outputs are  
290 used as the inputs for the MF-MHD model (Figure 1). In order to evaluate the effects of  
291 different crustal field orientations, plus various solar cycle and seasonal conditions on the  
292 Mars upper atmosphere ion loss, we study 18 standard cases plus four cases without crustal  
293 fields. The 18 cases combine three crustal field orientations (subsolar longitude, SSL=0°

294 W, 180° W, 270° W), three Martian seasons (aphelion, autumnal equinox, perihelion) with  
295 solar maximum (F10.7=200) and solar minimum (F10.7=70) conditions. Due to the fact  
296 that there is no significant difference between vernal equinox and autumnal equinox (the  
297 heliospheric distance difference between these two cases is not zero but small), we only  
298 study the latter. For all the cases, the solar wind density is set to  $4 \text{ cm}^{-3}$ , the upstream  
299 solar wind plasma temperature is set to  $3.5 \times 10^5 \text{ K}$ , the interplanetary magnetic field  
300 (IMF),  $B$ , is assumed to be a Parker spiral in the X-Y plane of MSO coordinate system  
301 with an angle of  $56^\circ$ , and the solar wind velocity is 400 km/s. Table 1 summarizes the  
302 cases studied in this paper.

303 The calculated ion escape rates (in  $\times 10^{24} \text{ s}^{-1}$ ) are summarized in Table 2 and the  
304 corresponding histograms are shown in Figure 4. The calculation of ion escape rate is  
305 conducted by integrals of the plasma density multiplied by the radial velocity component  
306 at the surface of a sphere far from the planet. Given the fact that the calculated ion  
307 escape rates do not change to any significant degree once the radius exceeds  $4 R_M$ , we  
308 select the integral spherical surface to be  $6 R_M$ . The results are quite interesting and  
309 several conclusions can be made.

### 3.1. Effects of crustal field orientation

310 First, the crustal magnetic field has a shielding effect to protect Mars from the solar wind  
311 interaction and is therefore able to reduce the ion escape rates. For example, comparison  
312 of cases in the AEQUUMIN conditions (cases 7-9) shows that case 8 (SSL=180°W, crustal  
313 field,  $B_c$ , mainly faces the Sun) has the smallest net ion escape rate ( $\text{O}^+$ ,  $\text{O}_2^+$  and  $\text{CO}_2^+$ )  
314 and case 7 (SSL=0°W,  $B_c$  mainly faces the tail region) has the largest net ion escape rate  
315 among these three cases. Interestingly, the same conclusion is not valid for aphelion and

316 perihelion conditions due to the axial tilt, inhomogenous distribution of the crustal field,  
317 and possibly the 3-D atmosphere profiles (e.g., the effect of surface albedo and thermal  
318 inertia in M-GITM). For aphelion conditions, even when SSL=180 (cases 2 and 5), the  
319 crustal magnetic field is mainly concentrated in the southern hemisphere polar region in  
320 the MSO coordinate system (as indicated by Figure 2). Therefore, the crustal field does  
321 not play a significant role in the solar wind Mars interaction like in the equinox cases.  
322 For perihelion conditions, when SSL=180 (cases 14 and 17), the crustal magnetic field  
323 is mainly concentrated in the dayside equatorial region (almost exactly facing the Sun).  
324 The shielding effect of the crustal field under this circumstance is stronger than those in  
325 the equinox cases.

326 Contrary to our initial expectation, the smallest net escape rate is associated with the  
327 AEQUUMIN conditions when the crustal magnetic field faces the Sun (case 8,  $1.53 \times 10^{24}$   
328  $\text{s}^{-1}$ ) instead of the APHMIN conditions with the same crustal field orientation (case 2,  
329  $2.12 \times 10^{24} \text{ s}^{-1}$ ). This behavior indicates that considering only the heliocentric distance or  
330 the associated chemical reaction rates is not sufficient to determine the ion escape rates  
331 due to the influence of the crustal magnetic field. According to our simulation, case 18  
332 (PERMAX, SSL=270) has the largest net ion escape rate,  $9.43 \times 10^{24} \text{ s}^{-1}$ . Although the  
333 existence of the axial tilt and the potential influence of the 3-D atmosphere can break  
334 the simple conclusion we draw for the equinox conditions, overall the crustal field shows  
335 a strong shielding effect to prevent the ion loss from the solar wind Mars interaction.  
336 It is interesting to point out that both hybrid models [e.g., *Brecht and Ledvina, 2014a*]  
337 and other MF-MHD codes [e.g., *Harnett and Winglee, 2006*] also showed that the crustal  
338 field has a strong shielding effect to protect Mars from the solar wind interaction regard-



339 less of different model setups and inputs. Meanwhile, *Riousset et al.* [2014] pointed out  
340 that the ionospheric outflows are likely to be prevented when the surface and lower at-  
341 mospheres are shielded by closed field lines due to the presence of magnetic loops and  
342 arcades. Such shielding ultimately reduces the fluxes of ions from the dynamo region to  
343 the upper ionosphere and thus reducing the ion escape rate. Furthermore, *Lundin et al.*  
344 [2011] studied how the ionospheric  $O^+$  outflow and escape are related to the crustal mag-  
345 netic field regions by analyzing the ASPERA-3 data from MEX. They found that a large  
346 fraction of the energized  $O^+$  ions remain magnetically trapped and are recycled within  
347 the mini-magnetospheres generated by the small-scale planetary crustal field regions at  
348 Mars. When the crustal field faces the sun, it has an effect to deviate the dayside ion flow  
349 and thus reducing the tailward transport and escape of ionospheric plasma.

### 3.2. Effects of seasonal variations

350 Second, by averaging over different crustal field orientations and solar cycle conditions,  
351 we found that aphelion conditions (APH) are associated with a net ion escape rate of  
352  $4.03 \times 10^{24} \text{ s}^{-1}$ , autumnal equinox conditions (AEQU) are associated with a net ion escape  
353 rate of  $4.40 \times 10^{24} \text{ s}^{-1}$ , and perihelion conditions (PER) yield an increased net ion escape  
354 rate up to  $5.37 \times 10^{24} \text{ s}^{-1}$ . As expected, perihelion has the largest net ion escape rate and  
355 aphelion has the smallest total ion loss rate. According to the values mentioned above,  
356 the seasonal variations may cause a factor of  $\sim 1.33$  variation in the ion loss rate.

357 Although we try to eliminate the effect of crustal field when estimating the ion escape  
358 affected by seasonal variations alone, the crustal field still has a potential effect on the  
359 results due to the axial tilt. In other words, the seasonal variations and crustal mag-  
360 netic field orientations are closely connected with each other, and may not be simply

361 decoupled by averaging over different  $B_c$  orientations and solar cycles. With different  
362 crustal field orientations but the same solar cycle and seasonal conditions, we calculated  
363 the ratio of maximum net ion loss to minimum ion loss for APHMIN (2.18/1.86~1.17),  
364 APHMAX (6.33/5.44~1.16), and the average of APHMIN and APHMAX, APH (~1.17);  
365 AEQUUMIN (2.24/1.53~1.46), AEQUUMAX (7.40/5.86~1.26) and AEQU (~1.36); PER-  
366 MIN (2.94/2.14~1.37), PERMAX (9.43/6.80~1.39) and PER (~1.38). Based on the  
367 results, we could easily prove that the shielding effect of crustal field are significantly  
368 correlated with season. Figure 4 may help to illustrate this conclusion in a more intuitive  
369 way. The crustal field has a more significant shielding effect for perihelion conditions than  
370 for the aphelion conditions due to the axial tilt.

371 In order to investigate the seasonal control of the ion loss more accurately, we calcu-  
372 lated four more cases without the crustal magnetic field: APHMIN, APHMAX, PERMIN  
373 and PERMAX, in which all SSL=180 °W. Surprisingly, we obtained a factor of ~ 1.29  
374 variation in the ion escape due to different seasons, which is only slightly smaller (within  
375 5%) than the previous estimate ~ 1.33, based on the average of results obtained with  
376 three crustal field orientations. Therefore, it may be appropriate to estimate the seasonal  
377 control of the ion loss by averaging over different crustal field orientations, but further  
378 investigations with more crustal field orientations or a real-time case are needed to verify  
379 this argument. Compared with the corresponding cases with crustal magnetic fields, all  
380 the ion escape rates increase (also see Figure 4) when crustal field is turned off, consistent  
381 with the first conclusion drawn above. On the other hand, the ion escape rate of case 18  
382 is generally higher than that of case 22, indicating that the crustal field may also help ions  
383 to escape from the Martian upper atmosphere under certain circumstances, e.g., magnetic

384 reconnection. The results may also be caused by the different M-GITM atmospheric pro-  
385 files (with different subsolar longitudes) used in these two cases. Currently, surface albedo  
386 and thermal inertia are the only two parameters implemented into M-GITM that can af-  
387 fect atmospheric profiles during Mars' rotation [Bougher *et al.*, 2015]. In other words, if  
388 one turns off these two parameters, all the atmospheric profiles are identical regardless of  
389 the subsolar longitude. Although these two parameters may affect the upper atmosphere  
390 profile to some extent, they are more important for the lower atmospheric structure via  
391 the radiative transfer process. At present, M-GITM does not include surface topography.

### 3.3. Effects of solar cycle conditions

392 Third, by averaging over different crustal field orientations and seasonal variations,  
393 we obtained that the net ion escape rate for solar maximum conditions (SOLARMAX,  
394  $7.06 \times 10^{24} \text{ s}^{-1}$ ) is about 3.3 times higher than that of solar minimum conditions (SO-  
395 LARMIN,  $2.14 \times 10^{24} \text{ s}^{-1}$ ). In other words, different solar cycles can affect the ion escape  
396 rate by a factor of  $\sim 3.3$  based on our simulations. Our calculated total ion escape rate  
397 for SOLARMIN conditions is  $\sim 2 \times 10^{24} \text{ s}^{-1}$ , in reasonable agreement with the MEX data  
398 as shown in Figure 4 in *Lundin et al.* [2013]. For SOLARMAX conditions, the calculated  
399 result is  $7.06 \times 10^{24} \text{ s}^{-1}$ , which is also reasonably consistent with the ion escape rate esti-  
400 mate from MEX data,  $\sim 1 \times 10^{25} \text{ s}^{-1}$  [Lundin *et al.*, 2013]. The increasing trend of the ion  
401 escape rate with solar activity is somewhat different from what reported by *Lundin et al.*  
402 [2013] (a factor of  $\sim 10$ ). One possible explanation is that we did not include the neutral  
403 wind in our simulations, which can greatly affect the ion loss [Brecht and Ledvina, 2014b].  
404 On the other hand, the recent paper published by *Ramstad et al.* [2015] showed that the  
405 solar wind density and velocity can greatly affect the ratio of escape rate between low and

406 high solar EUV conditions. They adopted more than seven years of ion flux measurements  
407 in the energy range 10 eV–15 keV from ASPERA-3/IMA instrument on board MEX. As  
408 shown in their Figure 5, it is clear that based on our simulation parameters (solar wind  
409 velocity 400 km and solar wind density  $4 \text{ cm}^{-3}$ ), the escape rate ratio is less than 10.

410 A careful analysis of individual mass spectra in *Lundin et al.* [2009] shows that the  
411  $\text{CO}_2^+$  contribution to the low-energy ( $< 300 \text{ eV}$ ) heavy ion outflow is  $\leq 10\%$ . On average,  
412 our  $\text{CO}_2^+$  ion contribution to the total ion escape ( $\text{O}^+$ ,  $\text{O}_2^+$  and  $\text{CO}_2^+$ ) is about 6.85% for  
413 SOLARMIN conditions and 5.30% for SOLARMAX conditions; both these values and  
414 the ratio from ALL conditions (as shown in Table 2,  $\sim 5.66\%$ ) are consistent with the  
415 observations ( $< 10\%$ ). *Nilsson et al.* [2011] pointed out that the average flux ratio of the  
416 molecular species ( $\text{O}_2^+$  and  $\text{CO}_2^+$ ) to  $\text{O}^+$  ions is  $0.9 \pm 0.1$  based on the statistics of MEX  
417 data from May 2007 to May 2011 for ion energies below 50 eV. Our escape rate ratio  
418 of molecular ( $\text{O}_2^+$  and  $\text{CO}_2^+$ ) to  $\text{O}^+$  ions varies case by case as shown in Table 2. Since  
419 the estimate by *Nilsson et al.* [2011] is based upon a four-year average, the calculated  
420 ratio should be independent of seasonal variations given the fact that one Martian year  
421 is approximately equal to two Earth's years. Based on our calculations, this ratio is  $\sim$   
422 4.16 for SOLARMIN conditions and 0.72 for SOLARMAX conditions. The average over  
423 solar cycles leads to a ratio of 1.04 (ALL conditions as shown in Table 2), in reasonable  
424 agreement with the MEX data. The MEX data used in previous studies [*Nilsson et al.*,  
425 2011] was collected only from low solar activity to moderate level, but our result is based  
426 on the average over two solar cycle conditions. The other important factor that can lead  
427 to a difference is that their estimate of the flux ratio was based on ion energies below  
428 50 eV, while our calculations include ions from all energy ranges. The low energy limit

429 in their calculation underestimates the high energy escape ions. It is noteworthy that  
430 although M-GITM and M-AMPS provide the MF-MHD code with more realistic 3-D  
431 cold and hot neutral atmosphere profiles (Figure 2 and Figure 3), currently there are few  
432 accurate measurements of the (thermal and suprathermal) oxygen profiles in the Mars  
433 atmosphere [Bougher *et al.*, 2014]. This uncertainty affects the calculated ion escape  
434 rates. Therefore, the neutral atmosphere profiles to be returned by the MAVEN mission  
435 will significantly reduce the uncertainty in calculated escape rates resulting from the lack  
436 of direct information regarding the cold and hot oxygen abundances.

437 Figure 5 shows a comparison of  $H^+$ ,  $O_2^+$  and  $O^+$  ion escape plumes in the  $x - z$  plane of  
438 the MSO coordinate system for two extreme cases: APHMIN (case 1) and PERMAX (case  
439 18). The main feature of the MF-MHD model is the asymmetric escape plume for heavy  
440 ion ( $O^+$ ,  $O_2^+$ ) species. The lack of significant escape plume for  $H^+$  ions is because of its  
441 small mass (and thus small gyroradius) and the fact that the solar wind and ionospheric  
442 protons are combined in the model [Najib *et al.*, 2011]. The plume provides a channel  
443 for ions to escape which cannot be reproduced by the multi-species MHD model [Ma  
444 *et al.*, 2004; Ma and Nagy, 2007]. The asymmetry is primarily caused by different Lorentz  
445 forces acting on each ion species [Najib *et al.*, 2011; Dong *et al.*, 2014]. From the particle  
446 simulation point of view, the asymmetry can also be explained by the induced electric  
447 field [Fang *et al.*, 2010; Curry *et al.*, 2013, 2014]. From Figure 5, it is not difficult to  
448 distinguish the aphelion case from the perihelion case according to the different strengths  
449 of the ion escape plume, primarily caused by different solar radiation. The upper panel is  
450 associated with aphelion conditions which has a weaker ion escape plume than the bottom  
451 panel for perihelion conditions, especially when focusing on the hot oxygen corona region

452 of the contour plot. The contour plots shown in Figure 5 are also consistent with the hot  
453 oxygen profiles shown in Figure 3 and the ion escape rates shown in Table 2.

### 3.4. Effects of mass differentiation

454 Last but not least, all the ion escape rates show a positive linear correlation with  
455 each other (Figure 6). The cold heavy ionospheric molecular ion escape fraction  $[(\text{O}_2^+$   
456  $\text{and/or CO}_2^+)/\text{Total}]$  is inversely proportional to the atomic ion escape fraction  $[\text{O}^+/\text{Total}]$ ,  
457 whereas  $\text{O}_2^+$  and  $\text{CO}_2^+$  ion escape fractions show a positive linear correlation (Figure 7).  
458 The escape fraction is defined as the escape rate ratio between an individual or sum of  
459 several ion species to total ions. The positive linear correlation in Figure 6 is mainly  
460 caused by the fact that an increase in solar irradiance leads to a higher amount of ionized  
461 gas via photoionization. Although the perfect linear anti-correlation in Figure 7 (d) is  
462 mathematically to be expected, all the linear correlations indicated in Figure 7 can also  
463 be physically interpreted. As we mentioned above, Mars has a solar cycle dependent  
464 hot atomic oxygen corona (see Figure 3), which is ionized by the solar radiation and  
465 the solar wind electrons via photoionization and electron impact ionization, respectively.  
466 The ionized  $\text{O}^+$  can be picked up by the solar wind and escape from the Martian upper  
467 atmosphere. The mass loading process reduces the solar wind speed and the dynamic  
468 pressure, and thus the solar wind has less chance to penetrate deep into the Martian  
469 ionosphere mainly due to the momentum conservation. As a result, the cold heavy iono-  
470 spheric molecular ions ( $\text{O}_2^+$  and  $\text{CO}_2^+$ ) are relatively less affected by the solar wind and  
471 the associated ion escape rate fraction  $[(\text{O}_2^+ + \text{CO}_2^+)/\text{Total}]$  is decreased. Besides, the  
472 ionized hot oxygen corona behaves approximately as a perfect conductor and therefore  
473 prevents the electric and magnetic fields from penetrating into the Martian ionosphere

474 to a certain degree. Both the mass loading and electromagnetic shielding contribute to  
475 the inverse correlation between the cold heavy ionospheric molecular ion escape fraction  
476  $[(\text{O}_2^+ \text{ and/or } \text{CO}_2^+)/\text{Total}]$  and the atomic ion escape fraction  $[\text{O}^+/\text{Total}]$ . Meanwhile,  $\text{O}_2^+$   
477 and  $\text{CO}_2^+$  ion escape fractions (ionospheric ion outflow) show a positive linear correlation  
478 (r-value=0.68) because both species are originated from the cold Martian ionosphere and  
479 should follow the same escape path. In order to avoid any artificial factor resulting from  
480 both the small datasets and missing the solar moderate cases, we decided to adopt the  
481 linear regression rather than a cubic polynomial regression fit to increase the correlation  
482 coefficient (r-value). In the future work, we plan to add the datasets from the solar mod-  
483 erate cases for the linear regression, most of which should lie in the middle of Figures 6  
484 and 7, and thus may help increase the r-value.

485 In Figures 6 and 7, the calculated ion escape rates and the ion escape rate fractions (with  
486 respect to the total ion loss) associated with solar minimum and solar maximum conditions  
487 are indicated by the red circle and blue square markers, respectively. The corresponding  
488 mean values are highlighted by the green markers with the same shape in both Figures.  
489 The least squares polynomial linear fit of the simulation results based on cases 1-18 (2  
490 average green points are not included) is shown in each figure as well. Correlations among  
491 different ion escape rates and the corresponding correlations among their fractions for  
492 different solar cycle conditions help us to understand the physics behind the regression  
493 lines. For example, during the period of high solar activity, Mars has a more extensive hot  
494 oxygen corona (see Figure 3), so the  $\text{O}^+$  ion escape fraction is relatively large in Figure  
495 7 (mainly distributed in the lower right corner when  $\text{O}^+/\text{Total}$  is the horizontal axis)  
496 while the cold heavy ionospheric molecular ion escape fraction is relatively small. The

497 associated statistical details, e.g., slope and intercept of the regression line, correlation  
498 coefficient (r-value), coefficient of determination (r-squared,  $R^2$ ), two-sided p-value and  
499 standard error of the estimate (stderr) are shown in Table 3.

500 The r-value is a measure of the linear correlation (dependence) between two variables  
501 X and Y, giving a value between +1 and -1, where 1 is total positive correlation, 0 is no  
502 correlation, and -1 is total negative correlation. It is defined as the (sample) covariance  
503 of the variables divided by the product of their (sample) standard deviations. The coef-  
504 ficient of determination, denoted  $R^2$  or  $r^2$ , is a number that indicates how well data fits  
505 a statistical model. Two-sided p-value indicates the probability of the correlation occur-  
506 ring by random chance. Standard error of the estimate (stderr) represents the average  
507 distance that the observed values fall from the regression line. Conveniently, it tells you  
508 how wrong the regression model is on average using the units of the response variable.  
509 Smaller values are better because it indicates that the observations are closer to the fit  
510 line. The linear correlation in Figures 6 and 7 is very useful when one does not have all  
511 the ion escape information and/or the spacecraft instrument mass resolution is not high  
512 enough to distinguish, e.g.,  $O^+$  and  $O_2^+$ . Knowing the total ion and  $O^+$  ion escape rates,  
513 the cold heavy ionospheric molecular ion escape rate can simply be calculated based on  
514 the linear fits shown in Figure 7 (d). If one needs to distinguish between  $O_2^+$  and  $CO_2^+$ ,  
515 the linear fit in the plot of  $CO_2^+$  versus  $O_2^+$  (Figure 6 (c)) can be used.

516 In addition to the comparison with the available MEX data, we also list our predictions  
517 here for the data to be returned by the MAVEN mission. Once the MAVEN datasets  
518 become available, we will conduct a detailed comparison between the three model results  
519 and MAVEN observational data. Such comparisons are essential to provide new insights by



520 coupling the three codes and to identify possible missing physics for future incorporation  
521 into the models. On the other hand, these 3-D simulations can provide global context  
522 for individual measurements; i.e. for example, predictions of the time history and certain  
523 physical problems of interest, based on the limited spacecraft data, are possible. It will  
524 be instructive to run a real-time case in the near future with the variable solar wind  
525 parameters (density and velocity) from the solar wind ion analyzer (SWIA) and the IMF  
526 from the magnetometer (MAG) instruments. Finally, investigators need to be careful  
527 when they calculate the controlling factors regulating the seasonal variations of the solar  
528 wind interaction. The coexistence of effects due to both crustal field location and the  
529 planetary axial tilt may influence the estimate to a certain degree.

#### 4. Conclusions

530 In summary, we studied the solar wind interaction with the Martian upper atmosphere  
531 by using one-way coupling of three comprehensive 3-D models, i.e., both the M-GITM  
532 thermosphere-ionosphere outputs and the M-AMPS exosphere hot atomic oxygen are used  
533 as inputs for the MF-MHD model. The effects of crustal field orientation, solar cycle and  
534 seasonal variations on the Martian upper atmosphere ion escape are investigated in detail  
535 by comparing 22 cases. Different solar cycles can affect the ion loss by a factor of  $\sim 3.3$ ,  
536 while different seasons can vary the ion loss by a factor of  $\sim 1.3$ . The coexistence of crustal  
537 field and axial tilt lead to a quite intricate solar wind-Mars interaction. There is no simple  
538 conclusion that a certain crustal magnetic field orientation can lead to the smallest ion  
539 escape rate as found in previous studies (e.g. *Ma and Nagy* [2007]). Instead, in this study,  
540 we found that the smallest ion escape rate also depends on the seasonal variations due  
541 to the axial tilt and the 3-D atmospheric structure. Overall, it is clear that the crustal

542 magnetic field has a shielding effect to protect Mars from the solar wind interaction,  
543 and this effect is the strongest for perihelion conditions with the crustal field facing the  
544 Sun. Furthermore, the cold heavy ionospheric molecular ion escape fraction  $[(\text{O}_2^+$  and/or  
545  $\text{CO}_2^+)/\text{Total}]$  is inversely proportional to the atomic ion escape fraction  $[\text{O}^+/\text{Total}]$ . On  
546 the other hand,  $\text{O}_2^+$  and  $\text{CO}_2^+$  ion escape fractions (ionospheric ion outflow) show a positive  
547 linear correlation.

548 Contrary to our initial expectation, the smallest total ion escape rate is associated with  
549 the autumnal equinox solar minimum (AEQUUMIN) case instead of the aphelion solar  
550 minimum (APHMIN) case, again due to the effect of coexisting crustal field and axial tilt  
551 plus the 3-D atmosphere. Based on averages over different solar cycles and various crustal  
552 field orientations, perihelion conditions yield the highest total ion escape rate and aphelion  
553 conditions yield the lowest total ion escape rate, which is well within our expectations.  
554 The calculated ion escape rates are in reasonable agreement with the recent observational  
555 data from MEX. For solar minimum conditions, the total ion ( $\text{O}^+$ ,  $\text{O}_2^+$  and  $\text{CO}_2^+$ ) escape  
556 rate is around  $2.0 \times 10^{24} \text{ s}^{-1}$  and for solar maximum conditions, the net ion loss is  $7.06$   
557  $\times 10^{24} \text{ s}^{-1}$ . By averaging our 18 MHD model cases, we obtained  $\text{CO}_2^+/\text{Total}$  ( $\sim 5.66\%$ )  
558 and  $(\text{CO}_2^+ + \text{O}_2^+)/\text{O}^+$  ( $\sim 1.04$ ), which are reasonably consistent with the statistical results  
559 from 4-year observational data.

560 This work aims to build a model library for the MAVEN mission, which has the potential  
561 to provide improved predictions of ion escape rates for comparison to future data to be  
562 returned by the MAVEN mission (2014-2016) and thereby improve our understanding of  
563 present escape processes. Estimates of ion escape rates over Mars history must start from

564 properly validated models that can be extrapolated into the past. This work will enhance  
565 the science return from the MAVEN mission.

566 **Acknowledgments.** This work was partially supported by NASA Earth and Space  
567 Science Fellowship NNX13AO56H, NASA/Colorado subcontract for MAVEN supporting  
568 generation of the model library NNH10CC04C, and NASA grant NNX13A031G. C.F.  
569 Dong also wants to acknowledge the MIPSE fellowship support from the Michigan In-  
570 stitute for Plasma Science and Engineering at the University of Michigan. Resources  
571 supporting this work were provided by the NASA High-End Computing (HEC) Program  
572 through the NASA Advanced Supercomputing (NAS) Division at Ames Research Cen-  
573 ter. The Space Weather Modeling Framework that contains the BATS-R-US code used in  
574 this study is publicly available from <http://csem.engin.umich.edu/tools/swmf>. For  
575 distribution of the model results used in this study, please contact the corresponding  
576 author.

## References

- 577 Acuña, M. H. et al. (1999), Global Distribution of Crustal Magnetization Discovered by  
578 the Mars Global Surveyor MAG/ER Experiment, *Science*, *284*, 790–793.
- 579 Arkani-Hamed, J. (2001), A 50-degree spherical harmonic model of the magnetic field of  
580 Mars, *Journal of Geophysical Research*, *106*, 23,197–23,208.
- 581 Barabash, S., A. Fedorov, R. Lundin, and J. A. Sauvaud (2007), Martian atmospheric  
582 erosion rates., *Science*, *315*, 501–503.
- 583 Bird, G. A., (1994), *Molecular Gas Dynamics and the Direct Simulation of Gas Flows*,  
584 2nd ed., Clarendon Press, Oxford.

- 585 Bougher, S. W., S. Engel, R. G. Roble, and B. Foster (2000), Comparative terrestrial  
586 planet thermospheres 3. Solar cycle variation of global structure and winds at solstices,  
587 *Journal of Geophysical Research*, *105*, 17669–17692.
- 588 Bougher, S. W., J. M. Bell, J. R. Murphy, M. A. Lopez-Valverde, and P. G. Withers  
589 (2006), Polar warming in the Mars thermosphere: Seasonal variations owing to changing  
590 insolation and dust distributions, *Geophysical Research Letters*, *33*, L02,203.
- 591 Bougher, S. W., P.-L. Blelly, M. R. Combi, J. L. Fox, I. Mueller-Wodarg, A. Ridley, and  
592 R. G. Roble (2008), Neutral Upper Atmosphere and Ionosphere Modeling, *Space Sci.*  
593 *Reviews*, *139*, 107-141.
- 594 Bougher, S. W., T. M. McDunn, K. A. Zoldak, and J. M. Forbes (2009), Solar Cycle  
595 Variability of Mars Dayside Exospheric Temperatures: Model Evaluation of Underlying  
596 Thermal Balances, *Geophysical Research Letters*, *36*, L05201.
- 597 Bougher, S. W., T. E. Cravens, J. Grebowsky, and J. Luhmann (2014), The Aeronomy of  
598 Mars: Characterization by MAVEN of the Upper Atmosphere Reservoir that Regulates  
599 Volatile Escape, *Space Science Reviews*, doi:10.1007/s11214-014-0053-7.
- 600 Bougher, S. W., D. J. Pawlowski, J. M. Bell, S. Nelli, T. McDunn, J. R. Murphy, M.  
601 Chizek, and A. Ridley (2015), Mars global ionosphere-thermosphere model (MGITM):  
602 Solar cycle, seasonal, and diurnal variations of the Mars upper atmosphere, *Journal of*  
603 *Geophysical Research*, doi:10.1002/2014JE004715.
- 604 Brain, D., et al. (2010), A comparison of global models for the solar wind interaction with  
605 Mars, *Icarus*, *206*, 139–151.
- 606 Brain, D., et al. (2012), Comparison of global models for the escape of martian atmospheric  
607 plasma, AGU Fall Meeting Abstracts, P13C-1969.

- 608 Brecht, S. H., and S. A. Ledvina (2014a), The role of the Martian crustal magnetic fields  
609 in controlling ionospheric loss, *Geophysical Research Letters*, *41*, 5340–5346.
- 610 Brecht, S. H., and S. A. Ledvina (2014b), Hybrid Particle Code Simulations of Mars:  
611 The Role of Assorted Processes in Ionospheric Escape, AGU Fall Meeting Abstracts,  
612 P54A-06.
- 613 Chamberlin, P. C., T. N. Woods, F. G. Eparvier (2008), Flare Irradiance Spectral Model  
614 (FISM): Flare component algorithms and results, *Space Weather*, *6*, S05001.
- 615 Cravens, T. E., J. U. Kozyra, A. F. Nagy, T. I. Gombosi, and M. Kurtz (1987), Electron  
616 impact ionization in the vicinity of comets, *Journal of Geophysical Research*, *92*, 7341–  
617 7353.
- 618 Curry, S. M., M. W. Liemohn, X.-H. Fang, Y.-J. Ma, J. Espley (2013), The influence of  
619 production mechanisms on pick-up ion loss at Mars, *Journal of Geophysical Research*,  
620 *118*, 554–569.
- 621 Curry, S. M., M. W. Liemohn, X.-H. Fang, Y.-J. Ma, J. Slavin, J. Espley, S. Bougher,  
622 and C. F. Dong (2014), Test particle comparison of heavy atomic and molecular ion  
623 distributions at Mars, *Journal of Geophysical Research*, *119*, 2328–2344.
- 624 Curry, S. M., J. G. Luhmann, Y. Ma, M. W. Liemohn, C. Dong, and T. Hara (2015), Com-  
625 parative pick-up ion distributions at Mars and Venus: Consequences for atmospheric  
626 deposition and escape, *Planet. Space Sci.*, doi:10.1016/j.pss.2015.03.026.
- 627 Deng, Y., A. D. Richmond, A. J. Ridley, and H.-L. Liu (2008), Assessment of the non-  
628 hydrostatic effect on the upper atmosphere using a general circulation model (GCM),  
629 *Geophysical Research Letters*, *35*, L01104.

- 630 Dong, C., S. W. Bougher, Y. Ma, G. Toth, A. F. Nagy, and D. Najib (2014), Solar wind  
631 interaction with Mars upper atmosphere: Results from the one-way coupling between  
632 the multifluid MHD model and the MTGCM model, *Geophysical Research Letters*, *41*,  
633 2708–2715.
- 634 Fang, X., M. W. Liemohn, A. F. Nagy, J. G. Luhmann, and Y. J. Ma (2010), On the effect  
635 of the martian crustal magnetic field on atmospheric erosion, *Icarus*, *206*, 130–138.
- 636 Feldman, P. D., A. J. Steffl, J. Wm. Parker, M. F. A’Hearn, J.-L. Bertaux, S. A. Stern, H.  
637 A. Weaver, D. C. Slater, M. Versteeg, H. B. Throop, N. J. Cunningham, L. M. Feaga  
638 (2011), Rosetta-Alice observations of exospheric hydrogen and oxygen on Mars, *Icarus*,  
639 *214*, 394–399.
- 640 Glocer, A., G. Tóth, Y. J. Ma, T. I. Gombosi, J. C. Zhang, and L. M. Kistler (2009),  
641 Multifluid Block-Adaptive-Tree Solar Wind Roe-Type Upwind Scheme: Magnetospheric  
642 composition and dynamics during geomagnetic storms—Initial results, *J. Geophys. Res.*,  
643 *114*, A12203.
- 644 Haberle, R. M., M. M. Joshi, J. R. Murphy, J. R. Barnes, J. T. Schofield, G. Wilson,  
645 M. Lopez-Valverde, J. L. Hollingsworth, A. F. C. Bridger, and J. Schaeffer (1999),  
646 General circulation model simulations of the Mars Pathfinder atmospheric structure  
647 investigation/meteorology data, *Journal of Geophysical Research*, *104*, 8957–8974.
- 648 Harnett, E. M., and R. M. Winglee (2006), Three-dimensional multifluid simulations of  
649 ionospheric loss at Mars from nominal solar wind conditions to magnetic cloud events,  
650 *J. Geophys. Res.*, *111*, A09213.
- 651 Johnson, R. E., J. G. Luhmann (1998), Sputter contribution to the atmospheric corona  
652 on Mars, *J. Geophys. Res.*, *103*, 3649–3653.

- 653 Kim, J., A. F. Nagy, J. L. Fox, and T. E. Cravens (1998), Solar cycle variability of hot  
654 oxygen atoms at Mars, *J. Geophys. Res.*, *103*, 29,339.
- 655 Lee, Y., M. R. Combi, V. Tenishev and S. W. Bougher (2013), Hot Oxygen Corona in  
656 Mars' Upper Thermosphere and Exosphere: A Comparison of Results using the MGITM  
657 and MTGCM, AGU Fall Meeting Abstracts, P21A-1703.
- 658 Lee, Y., M. R. Combi, V. Tenishev and S. W. Bougher (2014a), Hot carbon corona in  
659 Mars' upper thermosphere and exosphere: 1. Mechanisms and structure of the hot  
660 corona for low solar activity at equinox, *Journal of Geophysical Research*, *119*, 905–924.
- 661 Lee, Y., M. R. Combi, V. Tenishev and S. W. Bougher (2014b), Hot Carbon Corona in  
662 Mars' Upper Thermosphere and Exosphere: 2. Solar Cycle and Seasonal Variability,  
663 *Journal of Geophysical Research*, doi:10.1002/2014JE004669.
- 664 Luhmann, J. G., W. T. Kasprzak, and C. T. Russell (2007), Space weather at Venus and  
665 its potential consequences for atmosphere evolution, *Journal of Geophysical Research*,  
666 *112*, E04S10.
- 667 Lundin, R., S. Barabash, M. Holmström, H. Nilsson, M. Yamauchi, M. Fraenz, and E. M.  
668 Dubinin (2008), A comet-like escape of ionospheric plasma from Mars, *Geophysical*  
669 *Research Letters*, *35*, L18,203.
- 670 Lundin, R., S. Barabash, M. Holmström, H. Nilsson, M. Yamauchi, E. M. Dubinin, and  
671 M. Fraenz (2009), Atmospheric origin of cold ion escape from Mars, *Geophysical Re-*  
672 *search Letters*, *36*, L17202.
- 673 Lundin, R., S. Barabash, M. Yamauchi, H. Nilsson, and D. Brain (2011), On the relation  
674 between plasma escape and the Martian crustal magnetic field, *Geophysical Research*  
675 *Letters*, *38*, L02102.

- 676 Lundin, R., S. Barabash, M. Holmström, H. Nilsson, Y. Futaana, R. Ramstad, M. Ya-  
677 mauchi, E. M. Dubinin, and M. Fraenz, (2013), Solar cycle effects on the ion escape  
678 from Mars, *Geophysical Research Letters*, *40*, 6028–6032.
- 679 Ma, Y. J., A. F. Nagy, I. V. Sokolov, and K. C. Hansen (2004), Three-dimensional,  
680 multispecies, high spatial resolution MHD studies of the solar wind interaction with  
681 Mars, *Journal of Geophysical Research*, *109*, A07,211.
- 682 Ma, Y. J., and A. F. Nagy (2007), Ion escape fluxes from Mars, *Geophysical Research*  
683 *Letters*, *34*, L08,201.
- 684 Ma, Y. J., X. Fang, C. T. Russell, A. F. Nagy, G. Toth, J. G. Luhmann, D. A. Brain, and  
685 C. Dong (2014), Effects of crustal field rotation on the solar wind plasma interaction  
686 with Mars, *Geophysical Research Letters*, *41*, doi:10.1002/2014GL060785.
- 687 Modolo, R., G. M. Chanteur, and E. Dubinin (2012), Dynamic Martian magnetosphere:  
688 Transient twist induced by a rotation of the IMF, *Geophys. Res. Lett.*, *39*, L01106.
- 689 Najib, D., A. F. Nagy, G. Tóth, and Y. J. Ma (2011), Three-dimensional, multifluid, high  
690 spatial resolution MHD model studies of the solar wind interaction with Mars, *Journal*  
691 *of Geophysical Research*, *116*, A05,204.
- 692 Nilsson, H., N. J. Edberg, G. Stenberg, S. Barabash, M. Holmström, Y. Futaana,  
693 R. Lundin, and A. Fedorov (2011), Heavy ion escape from Mars, influence from so-  
694 lar wind conditions and crustal magnetic fields, *Icarus*, *215*, 475–484.
- 695 de Pater, I., and J. J. Lissauer (2010), *Planetary Sciences*, 2nd ed., Cambridge Univ.  
696 Press, New York, pp 5–6.
- 697 Powell, K. G., P. L. Roe, T. J. Linde, T. I. Gombosi, and D. L. De Zeeuw (1999), A  
698 Solution-Adaptive Upwind Scheme for Ideal Magnetohydrodynamics, *J. Computational*



- 699 *Phys.*, 154, 284–309.
- 700 Ramstad, R., S. Barabash, Y. Futaana, H. Nilsson, X.-D. Wang, M. Holmström (2015),  
701 The Martian atmospheric ion escape rate dependence on solar wind and solar EUV  
702 conditions I: Seven years of Mars Express observations, *Journal of Geophysical Research*,  
703 doi:10.1002/2015JE004816.
- 704 Ridley, A., Y. Deng, and G. Toth (2006), The global ionosphere-thermosphere model, *J.*  
705 *Atmos. Sol-Terr. Phys.*, 68, 839.
- 706 Rioussset, J. A., C. S. Paty, R. J. Lillis, M. O. Fillingim, S. L. England, P. G. With-  
707 ers, and J. P. M. Hale (2013), Three-dimensional multifluid modeling of atmospheric  
708 electrodynamics in Mars' dynamo region, *Journal of Geophysical Research*, 118, 1–13.
- 709 Rioussset, J. A., C. S. Paty, R. J. Lillis, M. O. Fillingim, S. L. England, P. G. Withers,  
710 and J. P. M. Hale (2014), Electrodynamics of the Martian dynamo region near magnetic  
711 cusps and loops, *Geophysical Research Letters*, 41, 1119–1125.
- 712 Schunk, R. W., and A. F. Nagy (2009), *Ionospheres*, 2nd ed., Cambridge Univ. Press,  
713 New York, pp102–109, chapter 8, pp 483.
- 714 Smith, M. D. (2004), Interannual variability in TES atmospheric observations of Mars  
715 during 1999–2003, *Icarus*, 167, 148–165.
- 716 Tenishev, V., and M. Combi (2008), A global kinetic model for cometary comae: The  
717 evolution of the coma of the Rosetta target comet Churyumov-Gerasimenko throughout  
718 the mission, *ApJ*, 685, 659–677.
- 719 Tóth, G. et al. (2012), Adaptive Numerical Algorithms in Space Weather Modeling, *J.*  
720 *Computational Phys.*, 231, 870–903.

- 721 Valeille, A., V. Tennishev, S. W. Bougher, M. R. Combi, and A. F. Nagy (2009), Three-  
722 dimensional study of Mars upper thermosphere/ionosphere and hot oxygen corona: 1.  
723 General description and results at equinox for solar low conditions, *Journal of Geophys-*  
724 *ical Research*, *114*, E11005.
- 725 Verigin, M. et al. (1991), Ions of planetary origin in the Martian magnetosphere (Phobos  
726 2/TAUS experiment), *Planetary and Space Science*, *39*, 131–137.

Author Manuscript

**Figure 1.** A sketch of a one-way coupling approach between M-GITM, M-AMPS and the MF-MHD model. The notation  $T_n$  denotes neutral atmosphere temperatures,  $[O]$ ,  $[CO_2]$ ,  $[O_{hot}]$  are the neutral O,  $CO_2$  and hot atomic oxygen number densities. Three photoionization processes are included. Here we focus on the one-way coupling indicated by the solid line. For the detailed study of one-way coupling between M-GITM and M-AMPS (dashed line), please refer to *Lee et al.* [2013, 2014a, b].

**Figure 2.** The neutral  $CO_2$  and O number densities shown on a sphere at an altitude of 220 km above the Martian surface from M-GITM for perihelion solar maximum (PERMAX) and aphelion solar minimum (APHMIN) conditions. Two coordinate systems are indicated in each plot: the Geographic (GEO) and the Mars-centered Solar Orbital (MSO) coordinate systems. The spherical contour plots are shown in the  $x - z$  plane (not a  $x - z$  cut) of both coordinates. The subsolar point is highlighted in each plot.

**Figure 3.** A comparison of the M-AMPS output hot oxygen number density (in  $\text{cm}^{-3}$ ) distribution between autumnal equinox solar minimum (AEQUMIN, case 7) and maximum (AEQUMAX, case 10) conditions (upper panel), and aphelion solar minimum (APHMIN, case 1) and perihelion solar maximum (PERMAX, case 16) conditions (bottom panel) in the  $x - z$  plane in the MSO coordinate system. All the results are based on the subsolar longitude,  $\text{SSL} = 0$ . Note the use of a logarithmic scale.

Author Manuscript

**Table 1.** Input parameters used for different calculations.

Simulation Cases	Subsolar Longitude (SSL)	Solar Cycle Conditions	Seasonal Variations
Case 1	0°W	Solar Minimum (APHMIN)	Aphelion (APH)
Case 2	180°W		
Case 3	270°W		
Case 4	0°W	Solar Maximum (APHMAX)	
Case 5	180°W		
Case 6	270°W		
Case 7	0°W	Solar Minimum (AEQUMIN)	Autumnal Equinox (AEQU)
Case 8	180°W		
Case 9	270°W		
Case 10	0°W	Solar Maximum (AEQUMAX)	
Case 11	180°W		
Case 12	270°W		
Case 13	0°W	Solar Minimum (PERMIN)	Perihelion (PER)
Case 14	180°W		
Case 15	270°W		
Case 16	0°W	Solar Maximum (PERMAX)	
Case 17	180°W		
Case 18	270°W		
Case 19	180°W	APHMIN	Aphelion and Perihelion comparison with crustal magnetic field turned off
Case 20	180°W	APHMAX	
Case 21	180°W	PERMIN	
Case 22	180°W	PERMAX	

**Table 2.** Calculated ion escape rates (in  $\times 10^{24} \text{ s}^{-1}$ ).

Simulation Cases	O <sup>+</sup>	O <sub>2</sub> <sup>+</sup>	CO <sub>2</sub> <sup>+</sup>	Total	(O <sub>2</sub> <sup>+</sup> + CO <sub>2</sub> <sup>+</sup> )/O <sup>+</sup>	CO <sub>2</sub> <sup>+</sup> /Total (%)
Case 1 (APHMINSSL0)	0.30	1.43	0.13	1.86	5.27	6.87
Case 2 (APHMINSSL180)	0.27	1.65	0.20	2.12	6.75	9.30
Case 3 (APHMINSSL270)	0.32	1.70	0.17	2.18	5.90	7.67
1-3 average (APHMIN)	0.30	1.59	0.16	2.05	5.95	7.99
Case 4 (APHMAXSSL0)	3.08	2.84	0.38	6.29	1.04	5.98
Case 5 (APHMAXSSL180)	2.64	2.38	0.41	5.44	1.06	7.63
Case 6 (APHMAXSSL270)	3.17	2.72	0.44	6.33	1.00	6.92
4-6 average (APHMAX)	2.96	2.64	0.41	6.02	1.03	6.81
1-6 average (APH)	1.63	2.12	0.29	4.03	1.48	7.11
Case 7 (AEQUMINSSL0)	0.41	1.68	0.15	2.24	4.42	6.90
Case 8 (AEQUMINSSL180)	0.31	1.12	0.11	1.53	4.01	6.89
Case 9 (AEQUMINSSL270)	0.44	1.45	0.13	2.02	3.60	6.46
7-9 average (AEQUMIN)	0.39	1.42	0.13	1.93	4.00	6.74
Case 10 (AEQUMAXSSL0)	4.57	2.52	0.26	7.35	0.61	3.49
Case 11 (AEQUMAXSSL180)	3.81	1.80	0.24	5.86	0.54	4.16
Case 12 (AEQUMAXSSL270)	4.99	2.17	0.24	7.40	0.48	3.25
10-12 average (AEQUMAX)	4.46	2.17	0.25	6.87	0.54	3.59
7-12 average (AEQU)	2.42	1.79	0.19	4.40	0.82	4.29
Case 13 (PERMINSSL0)	0.49	1.63	0.13	2.25	3.55	5.67
Case 14 (PERMINSSL180)	0.49	1.51	0.14	2.14	3.34	6.57
Case 15 (PERMINSSL270)	0.71	2.06	0.17	2.94	3.16	5.79
13-15 average (PERMIN)	0.56	1.73	0.15	2.44	3.33	5.98
Case 16 (PERMAXSSL0)	5.07	3.08	0.48	8.63	0.70	5.56
Case 17 (PERMAXSSL180)	4.02	2.40	0.38	6.80	0.69	5.62
Case 18 (PERMAXSSL270)	5.51	3.39	0.53	9.43	0.71	5.64
16-18 average (PERMAX)	4.86	2.96	0.46	8.29	0.70	5.61
13-18 average (PER)	2.71	2.35	0.31	5.37	0.98	5.69
1-3 & 7-9 & 13-15 average (SOLARMIN)	0.42	1.58	0.15	2.14	4.16	6.85
4-6 & 10-12 & 16-18 average (SOLARMAX)	4.10	2.59	0.37	7.06	0.72	5.30
1-18 average (ALL)	2.26	2.08	0.26	4.60	1.04	5.66
Case 19 (APHMINSSL180 [no B <sub>c</sub> ])	0.46	2.13	0.20	2.79	5.09	7.27
Case 20 (APHMAXSSL180 [no B <sub>c</sub> ])	3.13	2.69	0.43	6.26	1.00	6.94
19-20 average (APH [no B <sub>c</sub> ])	1.79	2.41	0.32	4.52	1.52	7.04
Case 21 (PERMINSSL180 [no B <sub>c</sub> ])	0.71	2.24	0.23	3.19	3.47	7.29
Case 22 (PERMAXSSL180 [no B <sub>c</sub> ])	5.41	2.51	0.56	8.48	0.57	6.58
21-22 average (PER [no B <sub>c</sub> ])	3.06	2.38	0.40	5.84	0.90	6.78

**Figure 4.** The histograms of ion escape rates (in  $\text{s}^{-1}$ ). Upper panel: cases with solar minimum conditions; middle panel: cases with solar maximum conditions; bottom panel: average cases. Noted that the ion escape rate scales in these three plots are different.

**Figure 5.** The calculated ion number densities in  $\text{cm}^{-3}$  in the  $x - z$  plane for  $\text{H}^+$ ,  $\text{O}_2^+$ , and  $\text{O}^+$  in a logarithmic scale. Case 1 is shown in the upper panels and case 18 is shown in the bottom panels. Noted that the logarithmic scales in different plots are different. The direction of the solar wind is parallel to the  $x$ -axis and in the  $-x$  direction.

**Figure 6.** Least squares polynomial linear fit of the simulation results based on cases 1-18. The calculated ion escape rates associated with solar minimum and solar maximum conditions are indicated by the red circle and blue square markers, respectively. The corresponding mean values are highlighted by the green markers with the same shape.

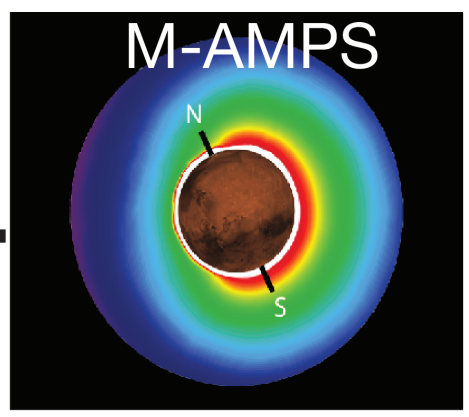
**Figure 7.** Least squares polynomial linear fit of the simulation results based on cases 1-18. The calculated ion escape rate fractions (with respect to the net ion loss) associated with solar minimum and solar maximum conditions are indicated by the red circle and blue square markers, respectively. The corresponding mean values are highlighted by the green markers with the same shape. Although the perfect linear anti-correlation in Figure 7 (d) is mathematically to be expected, all the linear correlations indicated in Figure 7 can also be physically interpreted.

**Table 3.** Slope and intercept of the regression line shown in Figure 7, correlation coefficient (r-value), coefficient of determination (r-squared,  $R^2$ ), two-sided p-value for a hypothesis test whose null hypothesis is that the slope is zero, standard error of the estimate (stderr).

	slope	intercept	r-value	$R^2$	p-value	stderr
$O_2^+ vs. O^+$	0.264	$1.49 \times 10^{24}$	0.833	0.694	$1.776 \times 10^{-5}$	0.0438
$CO_2^+ vs. O^+$	0.0553	$1.357 \times 10^{23}$	0.803	0.645	$5.949 \times 10^{-5}$	0.0103
$CO_2^+ vs. O_2^+$	0.204	$-1.647 \times 10^{23}$	0.937	0.878	$9.95 \times 10^{-9}$	0.019
$O_2^+ + CO_2^+ vs. O^+$	0.319	$1.626 \times 10^{24}$	0.835	0.698	$1.592 \times 10^{-5}$	0.0525
$O_2^+ vs. O^+$ (fraction)	-0.948	0.919	-0.999	0.997	$7.791 \times 10^{-22}$	0.0126
$CO_2^+ vs. O^+$ (fraction)	-0.052	0.081	-0.718	0.515	$8.015 \times 10^{-4}$	0.0126
$CO_2^+ vs. O_2^+$ (fraction)	0.052	0.033	0.680	0.462	$1.922 \times 10^{-3}$	0.014
$O_2^+ + CO_2^+ vs. O^+$ (fraction)	-1.0	1.0	-1.0	1.0	$5.027 \times 10^{-159}$	0.0

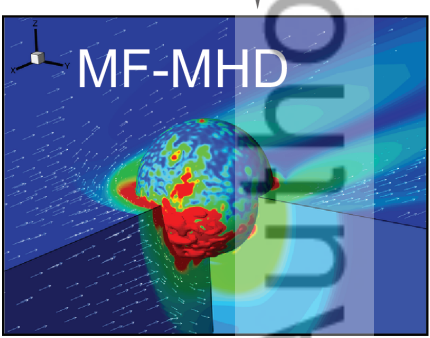


Author Manuscript

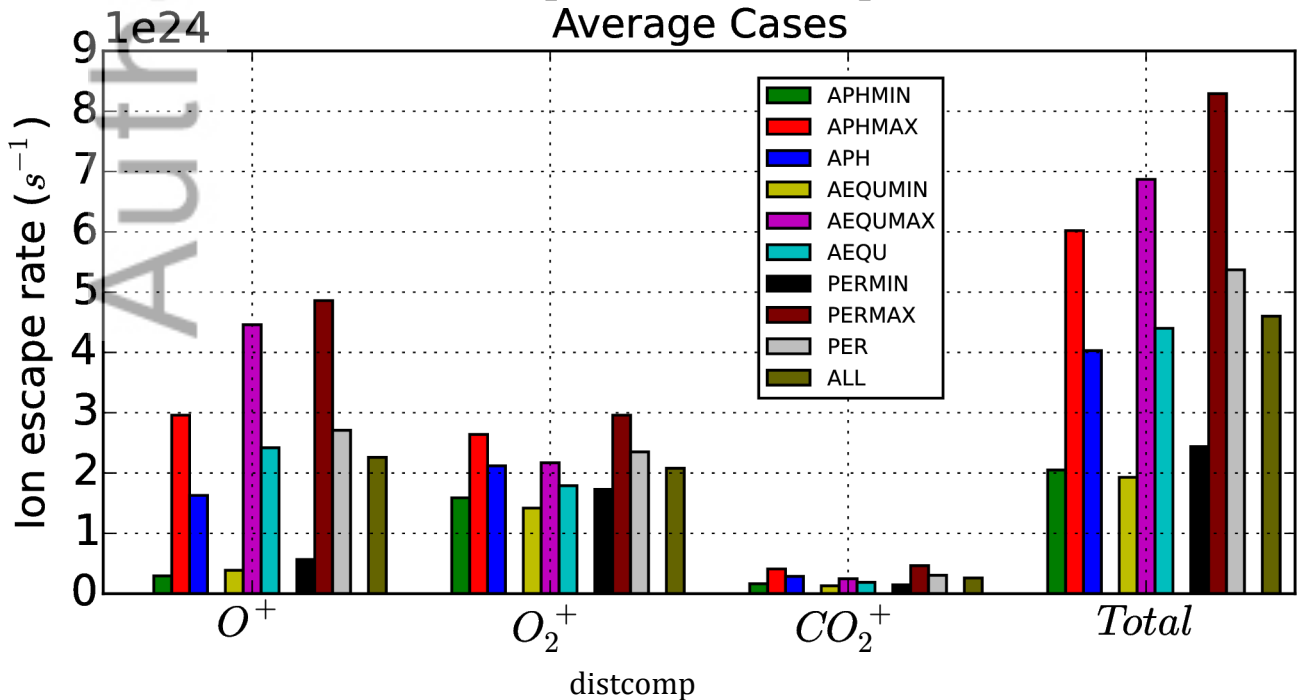
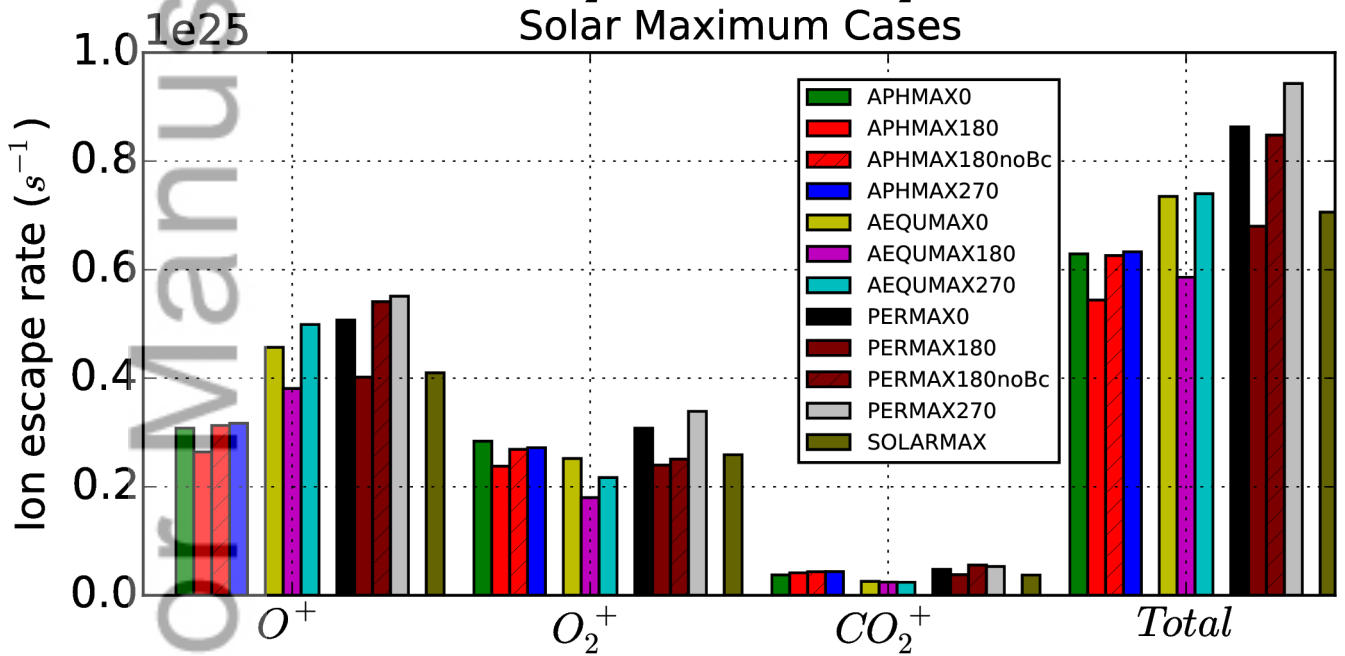
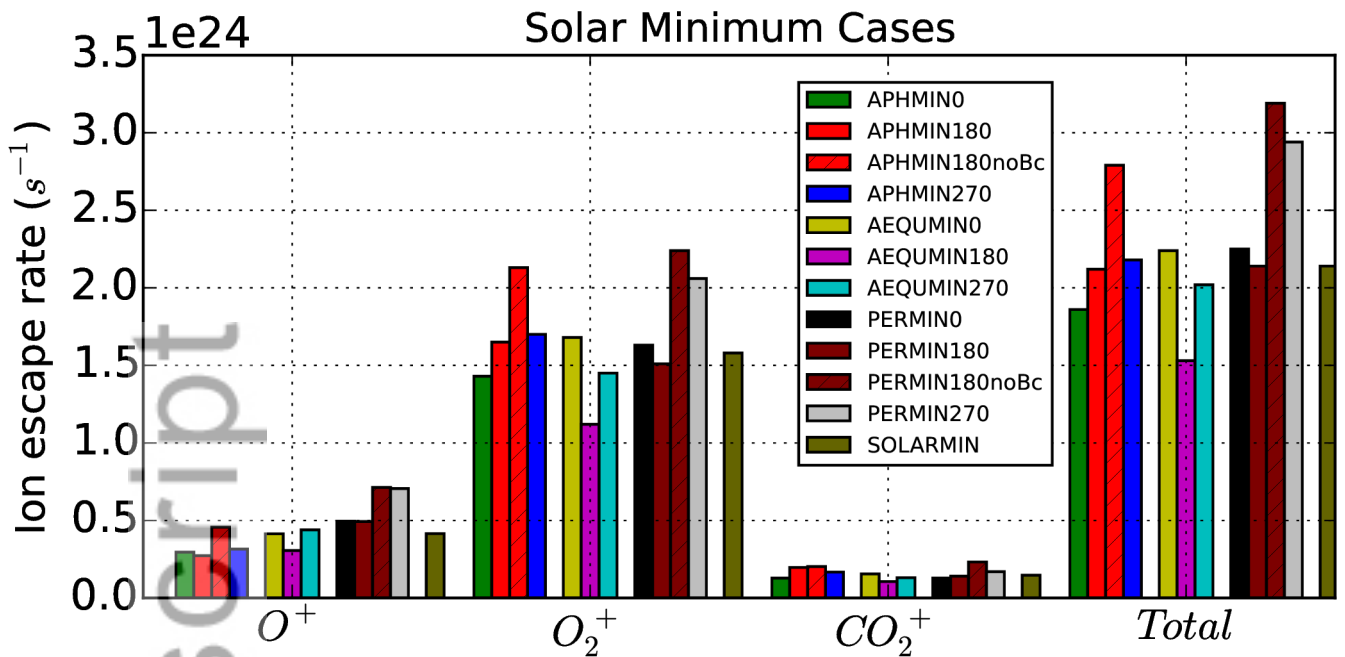


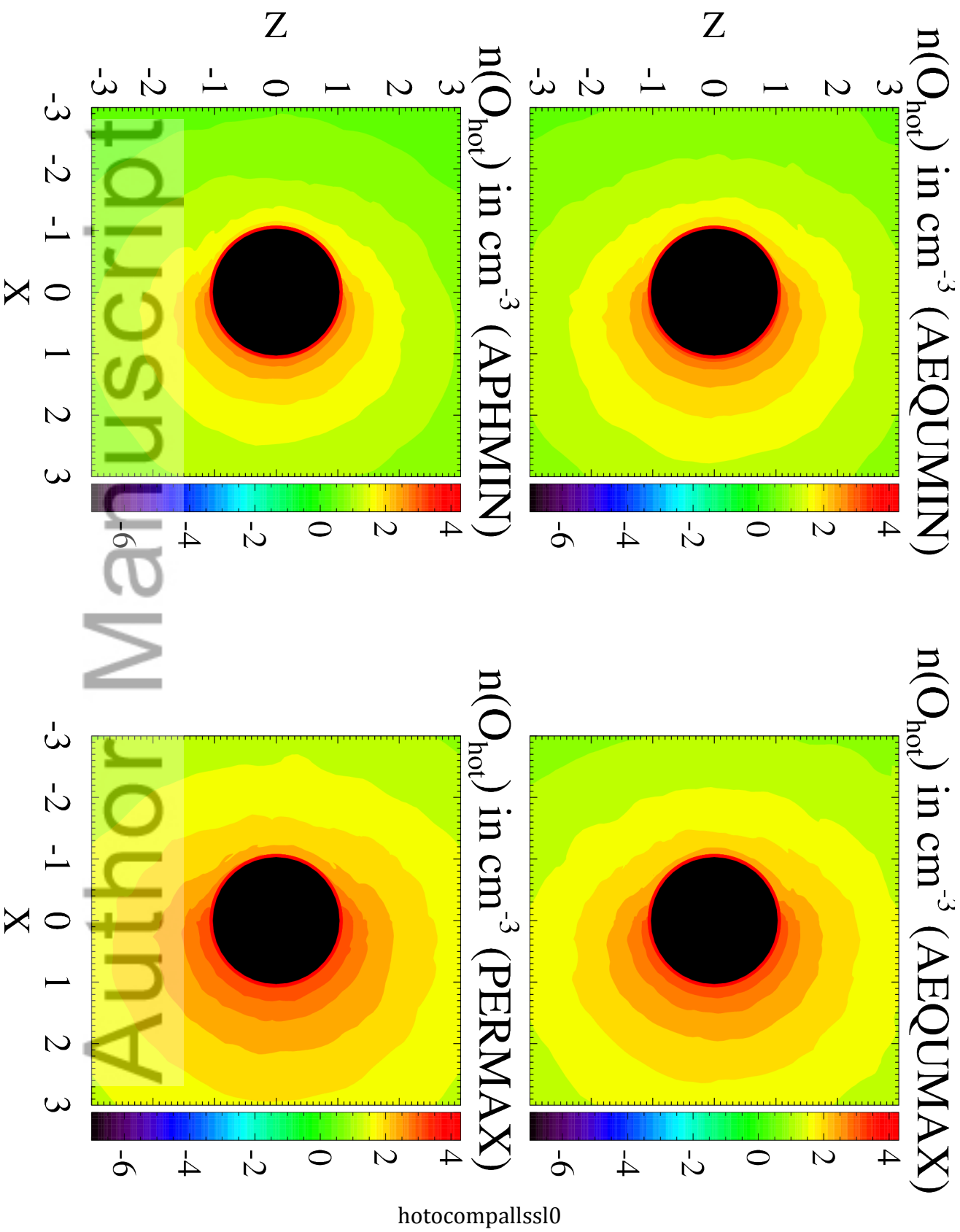
[O], [CO<sub>2</sub>], [CO],  
[N<sub>2</sub>], [O<sub>2</sub><sup>+</sup>],  
[e<sup>-</sup>], T<sub>e</sub>, T<sub>i</sub>, T<sub>n</sub>,  
U<sub>n</sub>, V<sub>n</sub>, W<sub>n</sub>

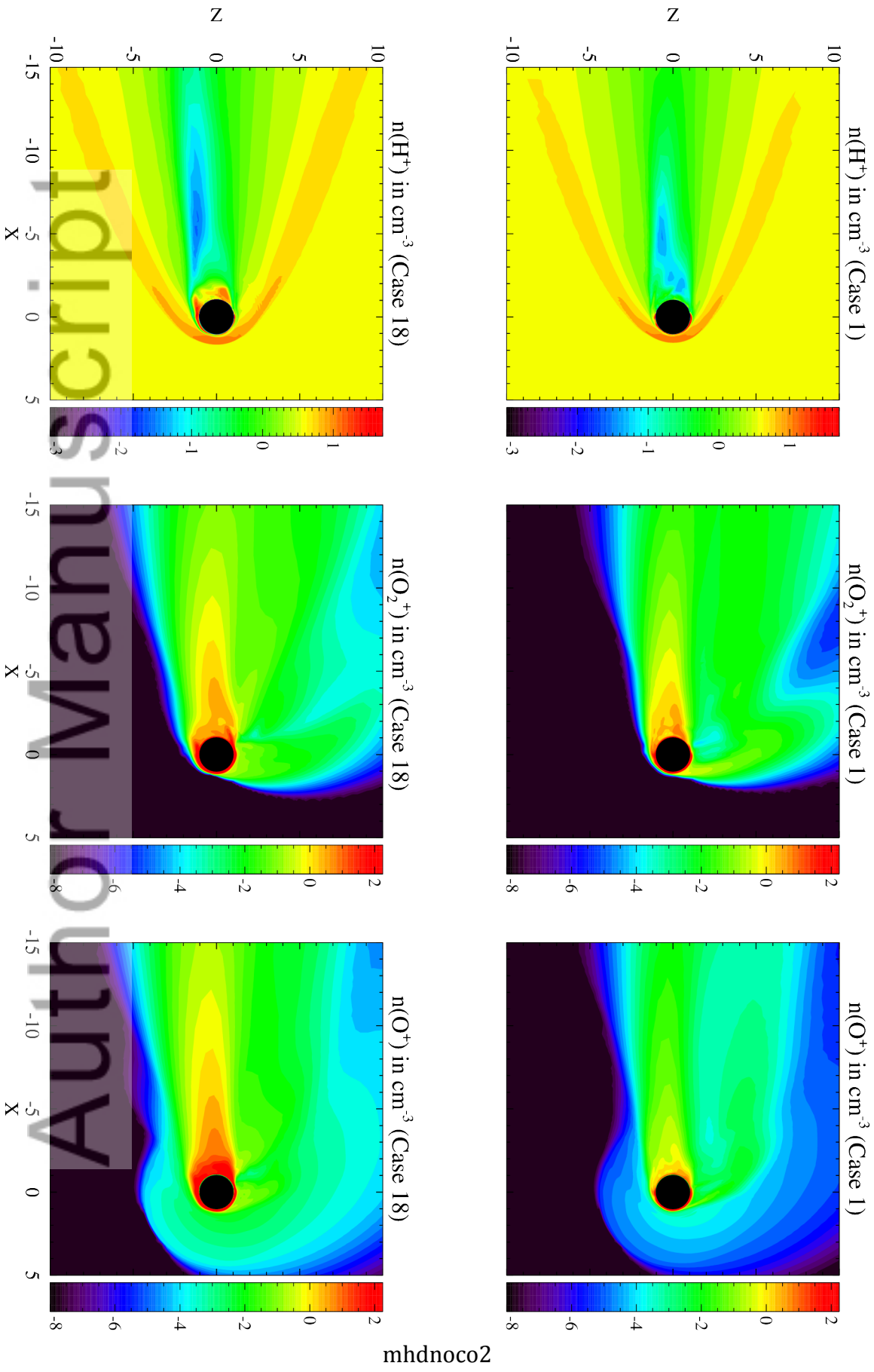
[O], [CO<sub>2</sub>], T<sub>n</sub>,  
Ionization frequencies  
(CO<sub>2</sub> → CO<sub>2</sub><sup>+</sup>, O → O<sup>+</sup>, CO<sub>2</sub> → O<sup>+</sup>)



coupling

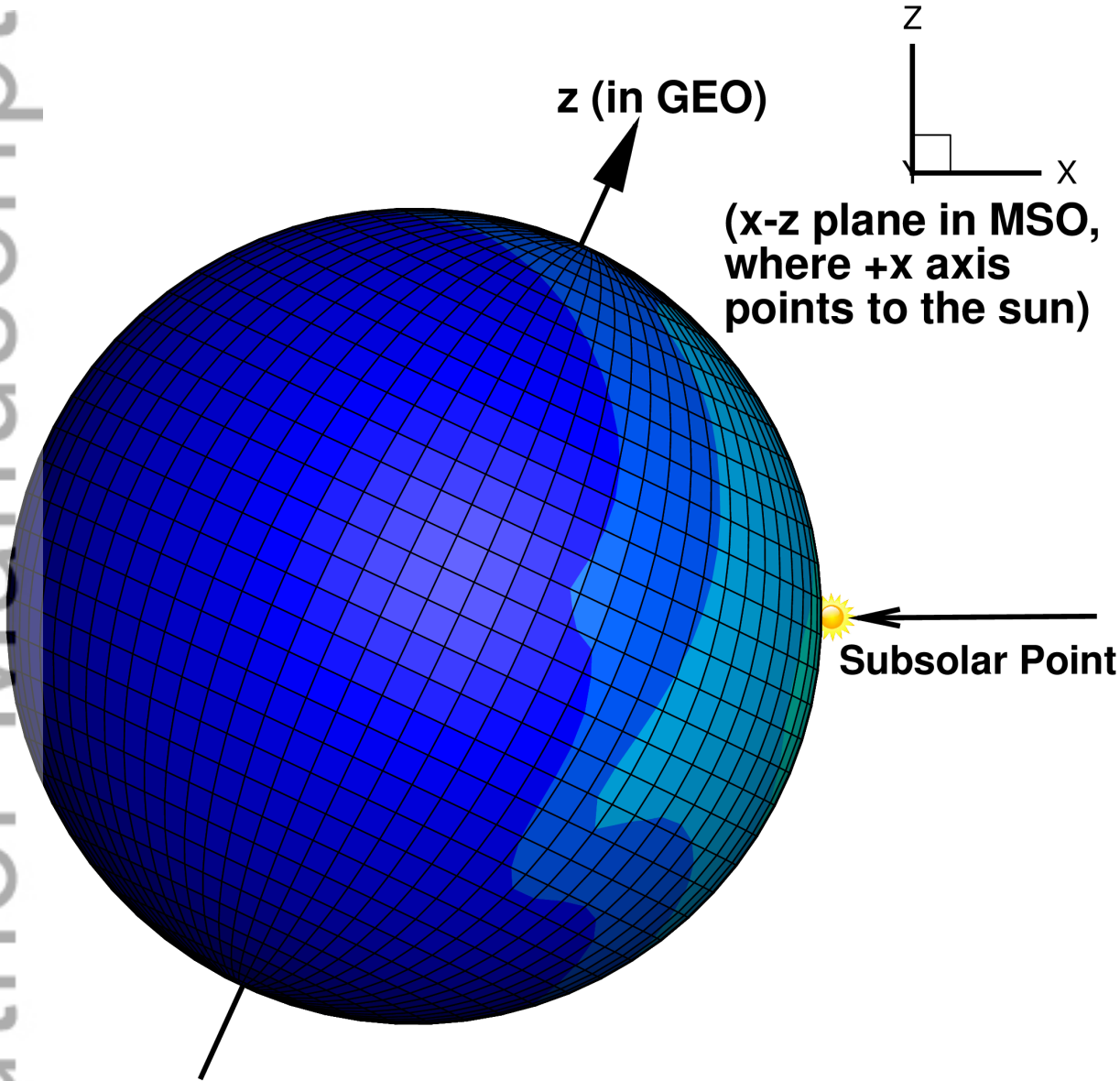
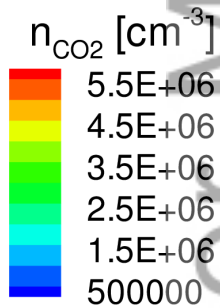






Author Manuscript

**CO<sub>2</sub>**  
**(APHMIN)**

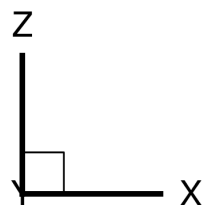


nco2aphmin

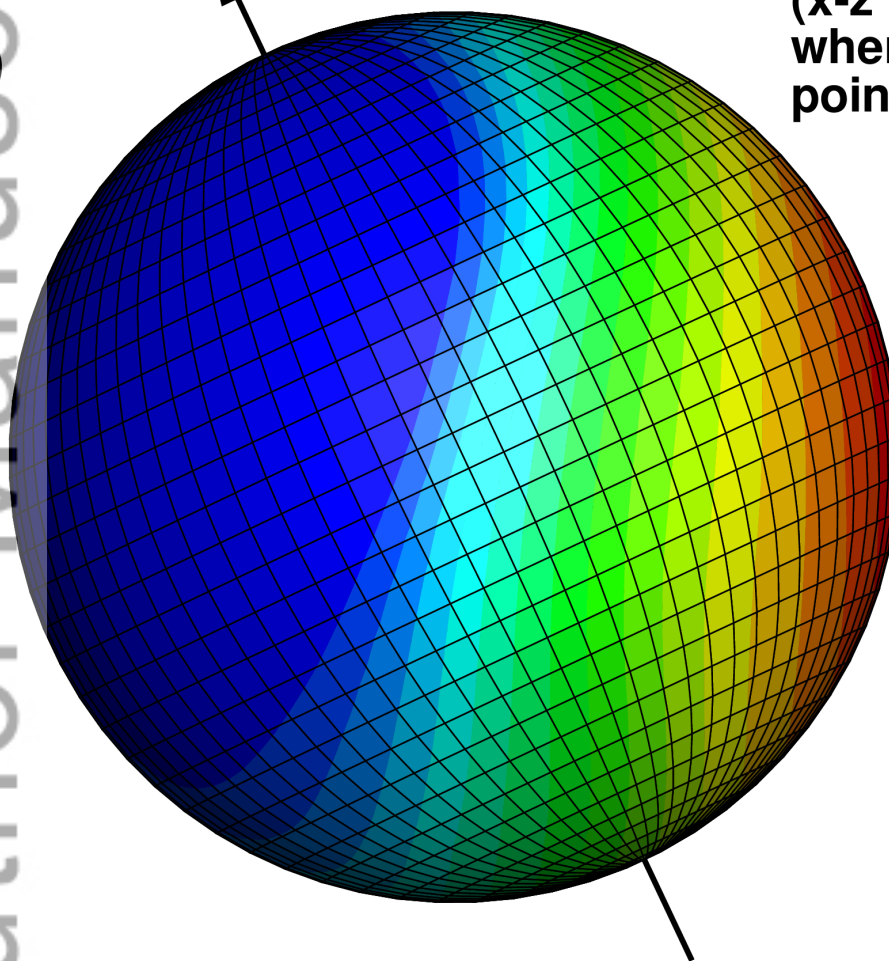
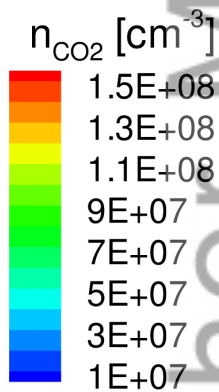
Author Manuscript


**CO<sub>2</sub>**  
**(PERMAX)**

**z (in GEO)**



**(x-z plane in MSO,  
where +x axis  
points to the sun)**

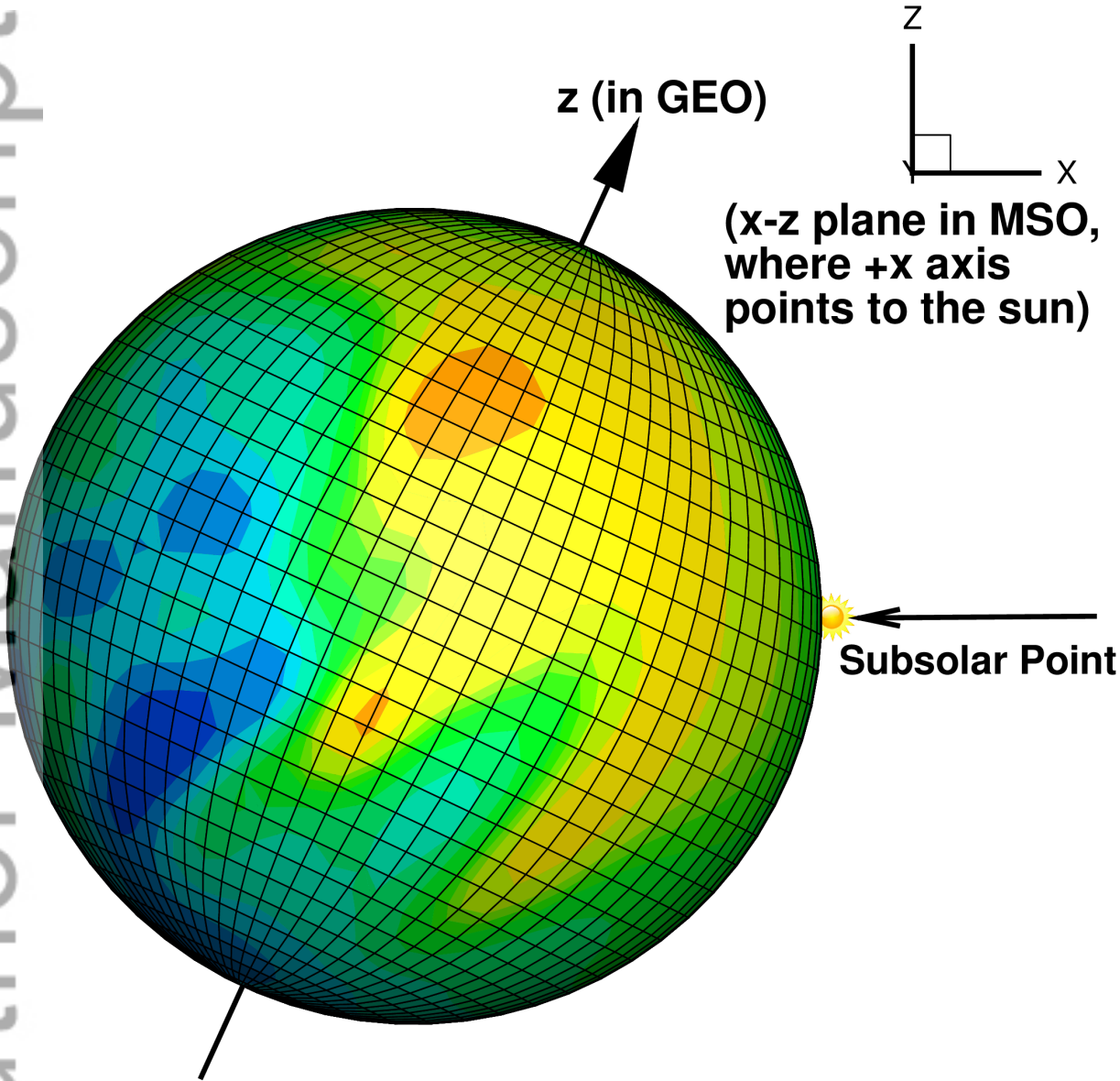
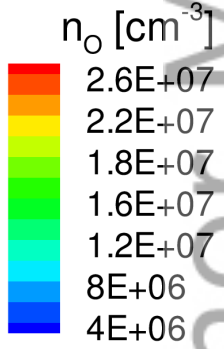


 **←**  
**Subsolar Point**

nco2permax

Author Manuscript

O  
(APHMIN)

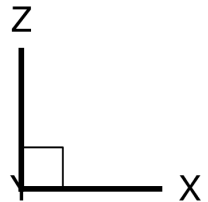


noaphmin

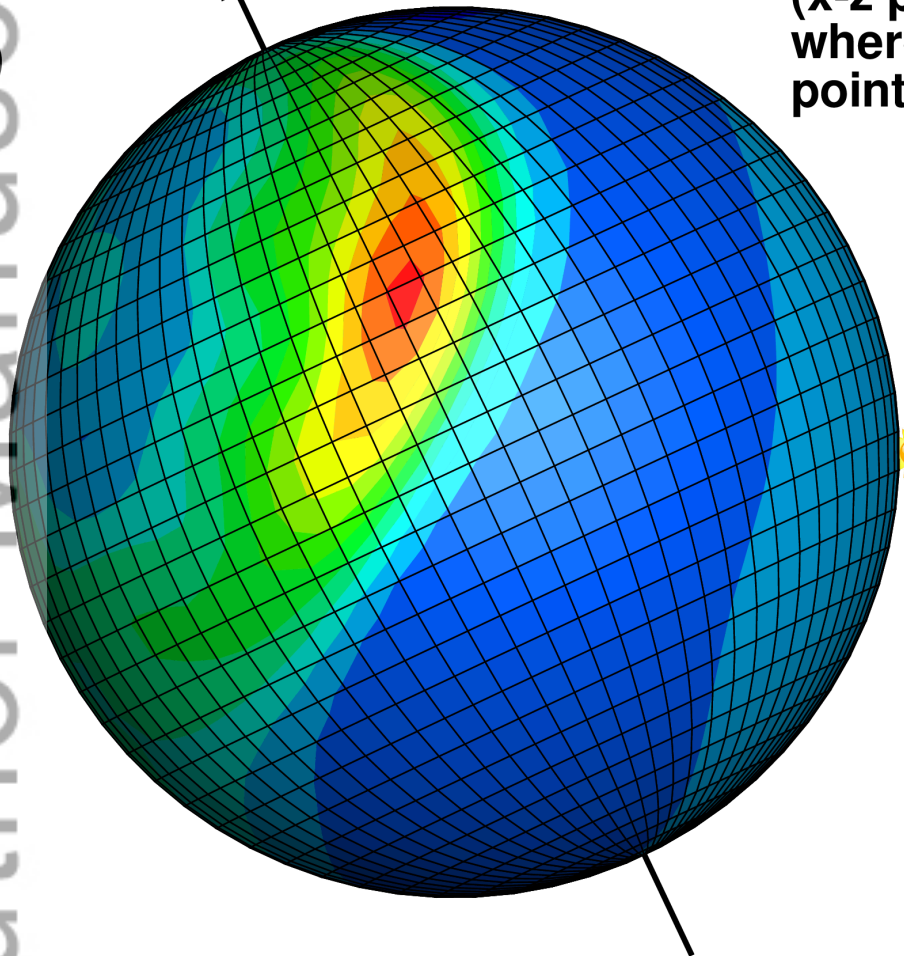
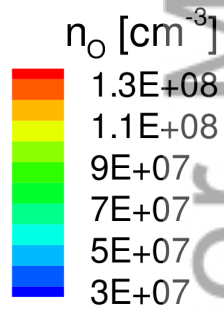
Author Manuscript

0  
(PERMAX)

z (in GEO)



(x-z plane in MSO,  
where +x axis  
points to the sun)

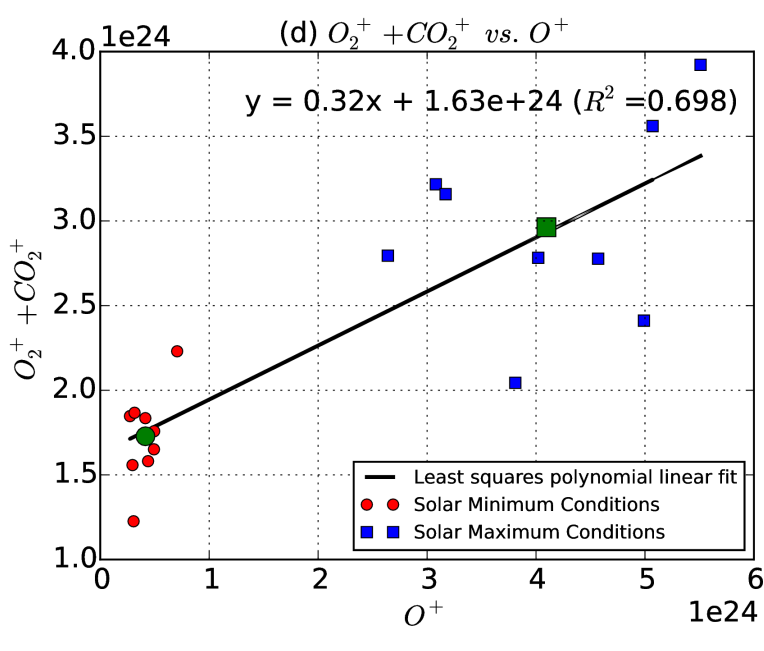
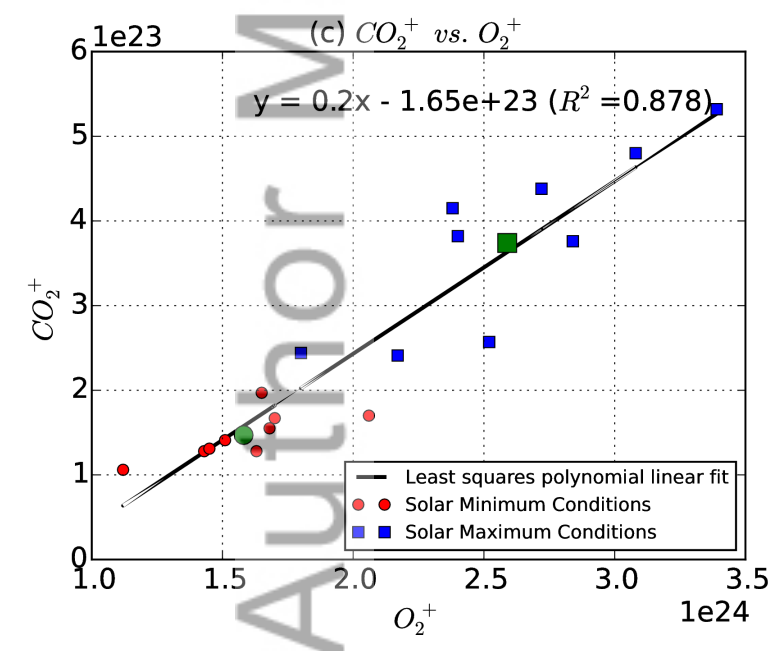
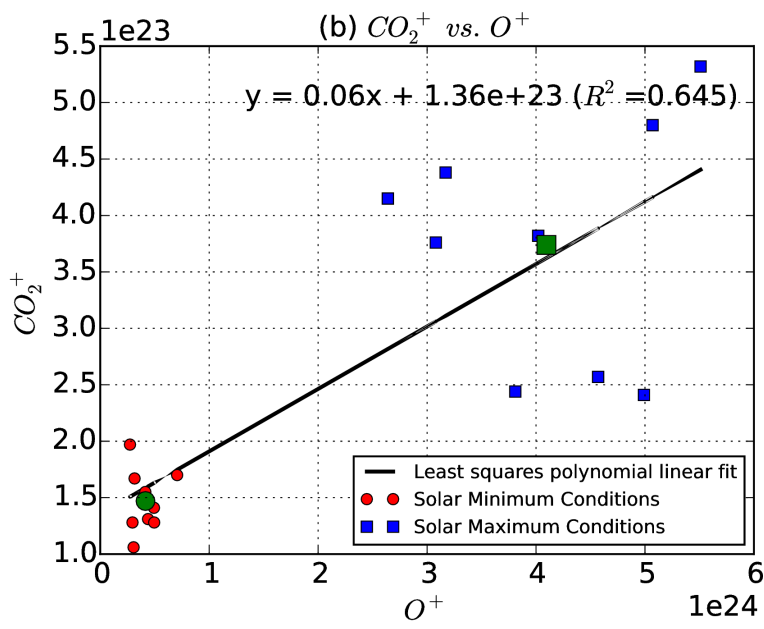
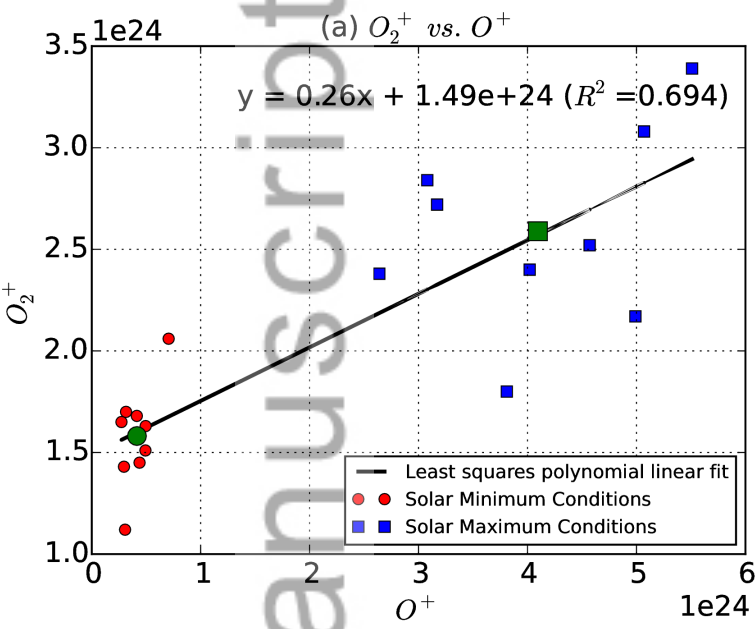


Subsolar Point

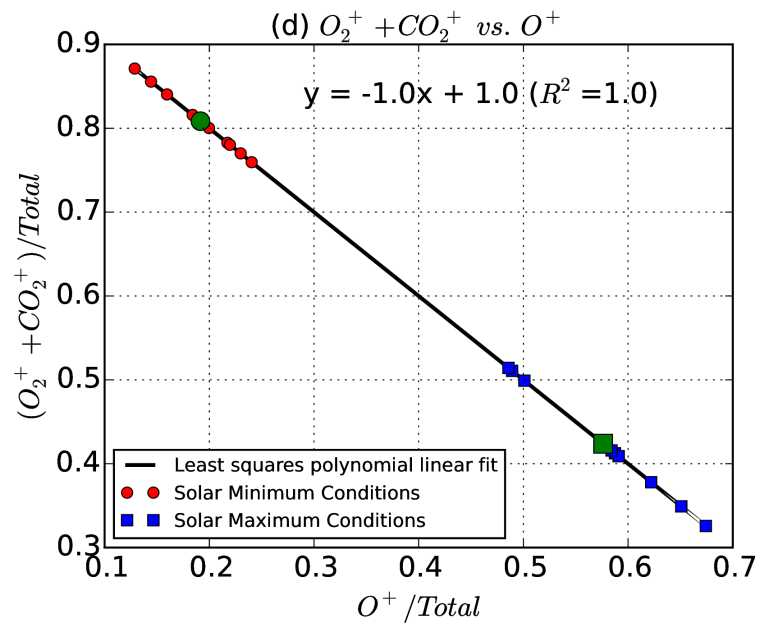
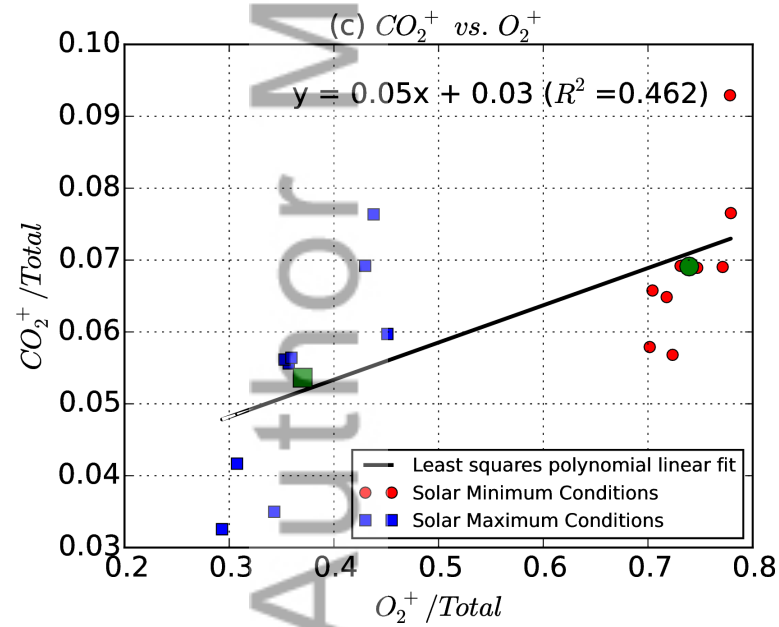
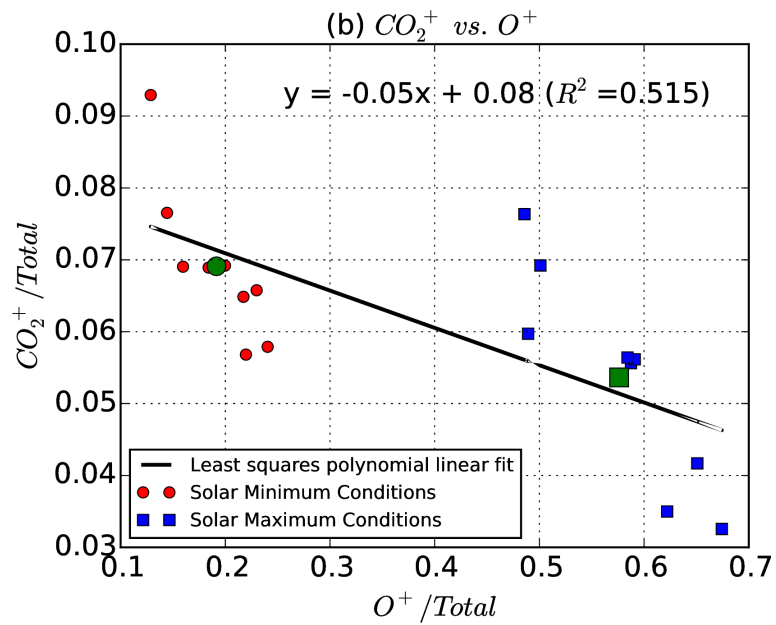
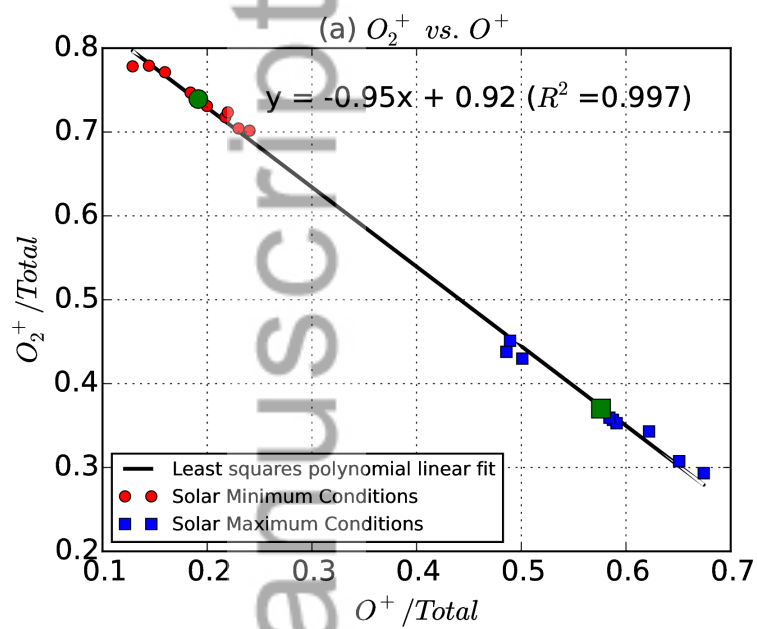
nopermax



Author Manuscript



scatter



scatter\_fraction